

# Numerical and experimental study on hydrodynamic performance of ships advancing through different canals

Khaled Elsherbiny<sup>1,2\*</sup>, Momchil Terziev<sup>2</sup>, Tahsin Tezdogan<sup>2</sup>, Atilla Incecik<sup>2</sup>, Mohamed Kotb<sup>1</sup>

<sup>1</sup>Department of Marine Engineering, College of Engineering and Technology, Arab Academy for Science, Technology and Maritime Transport, Abo Kir, Alexandria, P.O. Box 1029, Egypt

<sup>2</sup>Department of Naval Architecture, Ocean and Marine Engineering, Henry Dyer Building, University of Strathclyde, 100 Montrose Street, Glasgow G4 0LZ, UK

\*Corresponding author: [Khaled.elsherbiny@aast.edu](mailto:Khaled.elsherbiny@aast.edu), [Khaled.elsherbiny@strath.ac.uk](mailto:Khaled.elsherbiny@strath.ac.uk)

## Abstract

In international shipping, there are several waterways that are widely viewed as bottlenecks. Among these is the Suez Canal, where recent expansions have taken place. Although the Suez Canal has a high importance in international shipping, little research has been carried out in maximising the number of ships capable of traversing for a set period of time. The present study aims to examine hydrodynamic phenomena of ships advancing through the Suez Canal in the allowed speed range to determine the relative effects of the canal depth and /or width restrictions on the overall ship sailing performance. A rectangular canal is also included as a reference to gauge the effects of varying canal cross-section. The present study combines experimental, numerical, analytical and empirical methods for a holistic approach in calm water. As a case-study, the KCS hullform is adopted, and analysed experimentally, via Computational Fluid Dynamics, using the slender body theory, and empirical formulae. The results reveal strong coupling between the canal's cross section and all examined parameters.

## 1. Introduction

When a ship enters shallow waters, it has been observed that the distance between the keel of the ship and the seabed decreases as the speed increases, and on occasion, the ship has been known to strike the bottom. This phenomenon is known as 'ship squat' (Constantine, 1960). Because of the Bernoulli effect the free water surface around the ship drops. There is a vertical motion downwards and trim resulting in a decrease in the under-keel clearance (UKC). Thus all vessels squat as they move, even in deep water, although the magnitude of the squat is usually small. This phenomenon is a function of the shape of the hull and the forward speed through the water (Millward, 1996).

Ship squat is increased further when a vessel enters confined channels or rivers, since the velocity of water must increase due to the greater degree of restriction. Furthermore, a significant increase in resistance arises due to this hydrodynamic interaction. A drop in speed in the region of 30% can be expected upon entering shallow waters, which and may rise up to 60% if the ship is advancing through a confined channel such as a river or a canal (Barrass and Derrett, 2012).

Much research has been devoted to accurately predict ship squat, leading to a plethora of methods and approaches to the problem. Some of these are empirical methods, which are easy to use, but are reliable only for an early design stage (Barrass and Derrett, 2012; Rotteveel and Hekkenberg, 2015). Empirical formulae can quickly estimate the squat according to the ship dimensions, coefficients, speed, and underwater topology. These formulae are typically obtained from a series of model tests. Alternatively, analytical methods have been developed by researchers that make use of the assumptions inherent in potential flow theory such as slender body theory (Tuck, 1966). Namely, the flow is inviscid, irrotational and incompressible. Naturally, experimental investigations provide the most accurate results, and should be performed if possible (el Moctar et al., 2012; Zeraatgar et al., 2011). However, the availability of testing facilities, time required to perform the experiment, and the cost are highly prohibitive.

Finally, numerical, or Computational Fluid Dynamics (CFD) methods have been more recently developed and can be easily used for predicting ship squat. Although this approach has its own limitations, such as the computational cost, and knowledge required to perform a simulation, it is rapidly gaining popularity (Stern et al., 2013).

The present study combines all methods mentioned above. To elaborate, empirical formulae applicable in canal case-studies are used. The sinkage and trim of the ship are also analysed via the slender body theory as it is one of the most widely applied methods in this context. CFD simulations are also performed to replicate the experimental results and demonstrate the versatility of the numerical method. The analysis is performed on the KCS hullform, for which experimental data in shallow water is available for the specific case-studies examined herein (Elsherbiny et al., 2019b, 2019a).

This study is organised as follows. Section 2 presents the background of the methods used as part of this research. Section 3 contains the specific details relating to the implementation of each method. Section 4 is devoted to the obtained results and relevant discussion. Finally, the conclusion and recommendations for future work are given in Section 5.

## 2. Background

There are four main parameters influencing ship squat. These are the blockage factor ( $K$ ), the block coefficient ( $C_B$ ), the ship's velocity ( $V$ ), draft ( $T$ ) and water depth ( $h$ ). The blockage factor can be defined as the ratio of the submerged midship cross-sectional area and the underwater area of the canal or channel (Fig. 1). This dimensionless parameter is utilised in calculating ship squat by empirical formulations, and is shown in Eq. (1):

$$K = \frac{B \times T \times C_M}{W \times h} \quad (1)$$

where  $B$  is the ship's breadth,  $T$  is the ship's draft,  $W$  is the canal's breadth,  $C_M$  is the midship area coefficient and  $h$  is the water depth of the water.

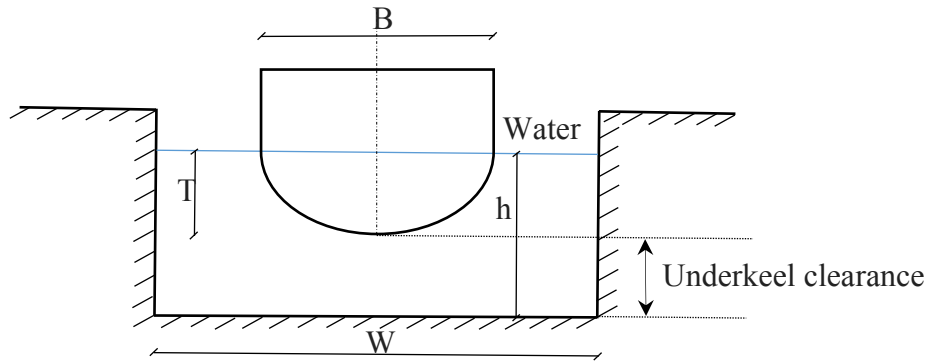


Figure 1. Ship in a canal

Michell (1898) developed a thin-body method to predict the wave resistance of a ship moving in shallow water. This method, henceforth referred to as the slender body theory, is based on fundamental assumption that the ship's beam is small compared to its length. As a consequence, the waves generated are also of small amplitude, which allows the linearisation of the free water surface. Later, Joukovski (1903) derived a similar formulation of the problem independently. The changes in a ship's wave pattern have been studied by Havelock (1924) for a point pressure impulse travelling over a free water surface. Havelock examined the wave patterns in shallow water by taking into account the speed of the vessel, and the depth of water, which led to the introduction of the depth Froude number ( $Fn_h$ ), Eq. (2).

$$Fn_h = \frac{v}{\sqrt{gh}} \quad (2)$$

where  $V$  is the speed of the vessel (m/s),  $g$  is the acceleration due to gravity ( $m/s^2$ ) and  $h$  is the water depth.

The depth Froude number can be thought of as the ratio of the ship's speed to the maximum wave velocity in shallow water of depth  $h$ . The well-known Kelvin wave pattern resulting from moving objects in water can be observed for  $Fn_h < 0.57$  (Tezdogan et al., 2015). As the ship's velocity increases, the angle between the wave pattern and the ship's centreline theoretically approaches 90 degrees until  $Fn_h$  becomes 1 (Tunaley, 2014), which is called the critical speed. When the depth Froude number is greater than one, the angle of the wave pattern begins to decrease again. The terms subcritical and supercritical speed are used for vessels propagating at  $Fn_h < 1$  and  $Fn_h > 1$ , respectively. Of greater practical interest is the former scenario, namely when the depth Froude number is smaller than 1 (Beck et al., 1975).

Many researchers have investigated ship squat in restricted water. Kreitner (1934) calculated ship squat using a one-dimensional hydraulic theory. He showed that the equation for the flow velocity in a canal ceases to provide reasonable solutions as the critical speed is approached. Constantine (1960) studied the different behaviour of ship squat for various ship speeds (subcritical, critical and supercritical), as well as the ratio of midship section to the cross section of the fairway. He determined that laterally restricted waterways have substantial effect on the

dynamic squat of a vessel. Inui (1954) investigated the effect of shallow water and restricted water on the wave-making resistance of ships. He concluded that higher degrees of discontinuity in the wave-resistance of a ship are caused by an increase in the restrictions of a waterway. This showed that the resistance itself is not a continuous function of depth Froude number in the case of restricted shallow waters. Tuck (1966) reproduced Michell's linearised slender body theory and explored the scenario where a ship is travelling in shallow water of constant, unrestricted width. Tuck (1966) solved for the hydrodynamic forces in shallow water to calculate the sinkage and trim for sub-critical speed ( $Fn_h < 1$ ) and super-critical speed ( $Fn_h > 1$ ) by using matched asymptotic expansions. He validated the results with model-scale experiments which showed good agreement for depth Froude number smaller than 0.7. However, the theory fails as depth Froude number approaches 1 because the formulations used become singular. Trim is the leading factor in the supercritical range, while sinkage is predominant in the subcritical range (Tuck 1966). The method predicts zero wave-making resistance in the subcritical range. Tuck (1967a) analysed the effect of restricted channel width in addition to depth on ship behaviour. Beck et al. (1975) expanded on the Tuck's work to account for vessels in dredged canals with an unrestricted shallow water region of constant depth extending infinitely on either side of the dredged section of the channel.

Gourlay (2008a) obtained a general Fourier transform method to calculate the sinkage and trim of a ship advancing in unrestricted shallow waters, canals and stepped channels as well as channels of arbitrary cross-section. He focussed on the subcritical range of motion. Gourlay (2008b) extended his modification of the Slender-body theory to calculate the sinkage and trim of a fast displacement catamaran propagating through horizontally unrestricted shallow water, which was valid for all speed regimes. Then, Gourlay (2008b) showed that trim, resistance and sinkage are affected by a change in the spacing between the catamaran hulls. In addition Gourlay (2009) used a theoretical method based on the linear superposition of slender-body shallow-water flow solutions to predict the sinkage and trim of two moving ships as they pass each other, either from opposite directions, or one ship overtaking the other.

Alderf et al. (2008) developed a new method for the numerical modelling of dynamic squat by using a finite element method. They also illustrated the effect of sea floor topology on a ship sailing at critical speed. Their model can give results for the dynamic responses of a ship in highly restricted canals on any seafloor shape. Alderf et al. (2008) developed their approach to validate the stability model as an extension of the method proposed by Janssen and Schijf (1953), who predicted the unstable squat positions for ships. Yao et al. (2011) produced and tested their theory for a Series 60 hull ( $C_B = 0.6$ ). They calculated the shallow water effects in terms of sinkage, trim, resistance and wave patterns for sub- and supercritical speeds on a ship by discretising the hull by a panel method. They distributed free and wall surface panels onto which Rankine sources of constant strength are mapped. Yao et al. (2011) validated their results with experimental data which showed good agreement.

Calisal and Alidadi (2011) performed a potential flow-based study to predict the squat of the Wigley hull. A slender-body theory approach was utilised to convert the three-dimensional problem into a series of 2-D cross sections distributed from the bow to the stern at equal

intervals. They applied a boundary element method sequentially to each cross section, which consisted of a solution to the summation of the disturbance and free-stream potentials. Thus, they obtained the velocity potential function expressing the problem at hand. To predict the ship squat, the pressure integration approach was used. This consists of integrating the pressure, acting on the hull to predict the hydrodynamic forces. To validate their theory, Calisal and Alidadi (2011) compared their predictions with experimental data. Interestingly, the comparison revealed that the predicted data does not deviate significantly from the experimentally predicted values at higher speeds. Instead, agreeable comparison was established for a range of depth Froude numbers from 0.2 to 0.4.

Lataire et al. (2012) conducted an experimental study for a model scale KVLCC2 to predict the squat for a wide range of water depths and widths of a canal with rectangular cross section. Ji et al. (2012) performed numerical simulations by solving the 3-D Navier-Stokes equations along with the standard  $k-\epsilon$  turbulence model. They simulated the wave patterns, induced by moving convoys composed of one or two barges in restricted waterways in order to predict the relationship between geometric and kinematic parameters, as well as the amplitude of ship-generated waves, and the water plane drawdown. Sergent et al. (2015) estimated the unstable equilibrium position of a ship during heave motions as a function of canal and ship parameters by using a new mathematical expression from a 2D analytical model. Tezdogan et al. (2016) predicted the squat and resistance of a model scale container ship advancing in a canal using a numerical method based on nonlinear unsteady RANS simulations.

Terziev et al. (2018) presented a numerical study to investigate the sinkage, trim and resistance of ships by using a scale model of the DTC container ship advancing through restricted shallow water in four channels with different cross sectional area and ship speeds. They used Computational Fluid Dynamics (CFD), the slender body theory and various empirical methods to calculate the trim and squat of the DTC advancing through different channel geometries.

Elsherbiny et al. (2019) conducted a series of experiments on a model of the KRISO Container Ship (KCS). The KCS performance was examined by measuring its sinkage, trim and total resistance. A wide range of water depth to ship draft ratios at various ship speeds were investigated. Additionally, the blockage effect was studied by varying the canal width. Also, the measured model resistance data was used to determine a form factor value for the KCS at various water depth to ship draft ratios. The estimation of experimental uncertainty was conducted for all tests. Later, Elsherbiny et al. (2019a) presented a series of model tests measuring the resistance, sinkage and trim variations with speed, water depth and loading conditions under different trim angles at 1:75 scale. This was done to examine the range of ship trim for safe and efficient sailing in restricted water in both depth and width, and to detect the best trim angle for ships sailing in restricted waters to reduce resistance and therefore fuel consumption.

Based on the above literature, the vast majority of studies focus on rectangular cross section canals. However, to the best of our knowledge, the Suez Canal has not been incorporated and assessed in any study using empirical, analytical, numerical and experimental techniques. The present paper will attempt to fill this gap by modelling the Suez Canal and a rectangular canal

for reference. The KCS hull form is modelled to advance through the aforementioned canals. To predict the wave resistance and form factor of the ship, CFD simulations are run in both multiphase and double body conditions. The details relating to each method are presented in the following section sequentially.

### **3. Empirical, analytical and numerical methods**

As referred to in Section 1, experimentation has several drawbacks. In an attempt to circumvent the use of expensive and time consuming physical model tests, researchers have developed a wide variety of tools. Naturally, each of these is associated with a set of assumptions and limitations. These assumptions and limitations are discussed in the following sections.

#### **3.1 Empirical methods**

Empirical methods are typically derived based on a regression technique, employed on a dataset. A common problem with this approach is that upon extrapolating variables beyond the range contained within the dataset introduces errors. The abovementioned dataset is usually experimental (Duffy, 2008). In the realm of ship hydrodynamics, the number of parameters, one must account for are high, rendering the problem difficult. A superimposed issue is that a slight alteration in any of the modelled (or otherwise) independent parameters induces a substantially different case-study than what the empirical method is suited for. For example, introducing a slope in the bathymetry changes the flow physics, versus a rectangular canal.

In the present context, the hullform is also of critical importance. Slight variations in the wetted area of the ship can have dramatic consequences in terms of the behaviour and performance of a ship (Tezdogan et al., 2016). Coincidentally, this is also the main motivation of hull form optimisation studies (Zhang et al., 2018a, 2018b, 2017). A change in depth or width also invalidates any analysis that was not performed using a similar set-up. This is the main problem of empirical methods: their predictions may be excellent for the case-study used in their inception, but this is far from the case when applied elsewhere. This drawback stems from the range and number of parameters required to describe the flow around a ship. A simple length to beam, draught, depth etc. ratio is insufficient to provide information on the actual flow characteristics. For our purposes, the Suez Canal is modelled as shown in Figure 2, and explained in the following section (Section 4.2).

As part of this research, we have employed several empirical formulae derived from experimental databases. Naturally, only those applicable to canal case-studies are examined. For a complete description of the mathematical background, the reader is referred to Briggs (2009, 2006), Briggs et al. (2013, 2009b), and Terziev et al. (2018). A description of the mathematical background of the empirical formulae is given in the Appendix.

#### **3.2 Slender body theory**

The slender body theory is one of the most successful approaches to computing shallow water trim and sinkage. This is particularly true in the low speed range, because viscous effects play a secondary role (Dand, 1967). The aforementioned theory, utilising a velocity potential

function, renders it unable to compute viscous contributions. As such, low speeds and moderate depths are well-suited for predictions using the slender body theory. In the present study, an in-house code which solves the equations of Tuck (1966), Tuck (1967), and Beck et al. (1975) is used. The debut of the code was presented in Terziev et al. (2019a) for dredged channels and canals. The method avoids integration of highly oscillatory integrals, representing the Fourier transform of the ship's cross-sectional area and beam (Gourlay, 2014; Tuck, 1967b) by using the convolution form of the governing equations (Tuck, 1967a, 1966). This is done because, as stated by Gourlay (2014), the convolution form of the equations is favourable for practical applications. The input data for KCS, as modelled for the slender body theory is shown in Figure 3 using a scale factor of 1:75. The principal characteristics of the ship are shown in Section 5.1.

The theory begins by supposing that the flow is two dimensional, and satisfies Laplace's equation:

$$(1 - Fn_h) \frac{\partial^2 \phi}{\partial x^2} + \frac{\partial^2 \phi}{\partial y^2} = 0 \quad (3)$$

where  $\phi$  is used to denote the velocity potential. For the cases examined here (subcritical speeds), the solutions of the above equation are elliptical. The boundary conditions are a critical component of the theory. The hull is described by

$$\frac{\partial(x+\phi)}{\partial n} = 0 \quad (4)$$

where  $\partial/\partial n$  is the derivative in the normal direction. This also holds for the seabed. To satisfy mass conservation, Tuck (1966) arrived at:

$$\frac{\partial \phi}{\partial x} = \pm \frac{V}{2h_0} S'(x) \text{ at } y = 0 \text{ i.e. at the hull} \quad (5)$$

where  $S(x)$  is the hull cross-sectional area at position  $x$ , and prime is used to denote the derivative  $dS/dx$ ,  $h_0$  is the interior water region depth, and  $V$  is the ship speed. The remaining boundary conditions are that the velocity potential must vanish at an infinite distance from the ship. To account for a change in depth, which characterises a dredged channel, Beck et al. (1975) split the flow into interior and exterior regions based on the depth:

$$h(y) \begin{cases} h_o, & |y| < w/2 \\ h_\infty, & |y| > w/2 \end{cases} \quad (6)$$

Where  $w$  is the width of the interior region. Splitting the domain thus creates two different flow regimes. The interior is characterised by the depth  $h_0$  and resulting interior depth Froude number  $F_0 = V/\sqrt{h_0 g}$ , and exterior depth Froude number  $F_\infty = V/\sqrt{h_\infty g}$ .

The solution proceeds by defining the functions  $k(x)$  and  $\theta$  as follows:

$$k(x) = \left[ \coth \frac{\pi x}{w \sqrt{1-F_0^2}} - 1 \right] \exp \left( \frac{2\theta w}{w \sqrt{1-F_0^2}} \right) \quad (7)$$

$$\theta = \begin{cases} \arctan\left(\frac{h_\infty\sqrt{F_\infty^2-1}}{h_0\sqrt{1-F_0^2}}\right) & \text{for } F_\infty < 1 \\ i \times \text{sgn}(k)\arctan\left(\frac{h_\infty\sqrt{1-F_\infty^2}}{h_0\sqrt{1-F_0^2}}\right) & \text{for } F_\infty > 1 \end{cases} \quad (8)$$

where  $i = \sqrt{-1}$  and  $\text{sgn}(k)$  is the signum of the Fourier transform variable  $k$ .

The only change between the open shallow water, dredged channel and canal cases are expressed by the  $\theta$  parameter and the ratio  $h_0/h_\infty$ . When  $\theta = 0$ , the above relationships reduce to the canal case-studies. Whereas when  $h_0/h_\infty = 1$ , the relationships reduce to their the open water variants (Beck et al., 1975).

The next step is to calculate the force and moment coefficients, which are predicted as shown in Eq. (9) and Eq. (10), respectively:

$$C_f = \frac{\int b(x)fs'(\xi)k(x-\xi)d\xi dx}{2wL\sqrt{1-F_0^2} \int b(x)dx} \quad (9)$$

$$C_m = \frac{\int xb(x)fs'(\xi)k(x-\xi)d\xi dx}{2wL\sqrt{1-F_0^2} \int b(x)x^2 dx} \quad (10)$$

Where  $fs'(\xi)k(x-\xi)d\xi dx$  is the convolution mentioned previously,  $f$  is used to denote the Cauchy or principle value integral and  $\xi$  is the convolution variable.

Once these are obtained, the solution requires the definition of two shape parameters,  $\alpha$  and  $\beta$  (Eq. (11) and Eq. (12)), which are used to predict the sinkage ( $C_S$ ) and trim ( $C_\theta$ ) coefficients, as demonstrated in Eq. (13) and Eq. (14), respectively.

$$\alpha = \frac{\int xb(x)dx}{L \int b(x)x^2 dx} \quad (11)$$

$$\beta = \frac{L \int b(x)x dx}{\int b(x)x^2 dx} \quad (12)$$

$$C_S = \frac{C_f - \alpha C_m}{1 - \alpha\beta} \quad (13)$$

$$C_\theta = \frac{C_m - \beta C_f}{1 - \alpha\beta} \quad (14)$$

Once the above parameters have been obtained, the sinkage ( $s$ ) and trim ( $t$ ) can be calculated:

$$s = \frac{LC_S F_0^2}{\sqrt{1-F_0^2}} [m] \quad (15)$$

$$t = \frac{C_\theta F_0^2}{\sqrt{1-F_0^2}} [radians] \quad (16)$$

In order to predict the parameters of interest in the modelled Suez Canal, the sloped shape is transformed into a rectangular cross-section with equal depth and blockage ratio (Gourlay, 2008a). This process is depicted in Figure 2a for the Suez Canal. The equivalent canal is characterised by a depth of 0.32m, and width equal to 2.89m. Then, the application of the abovementioned equations for a canal of constant width and depth are straightforward. This study will serve as a validation of the in-house code. For reference, the rectangular canal is modelled as depicted in Figure 2b.

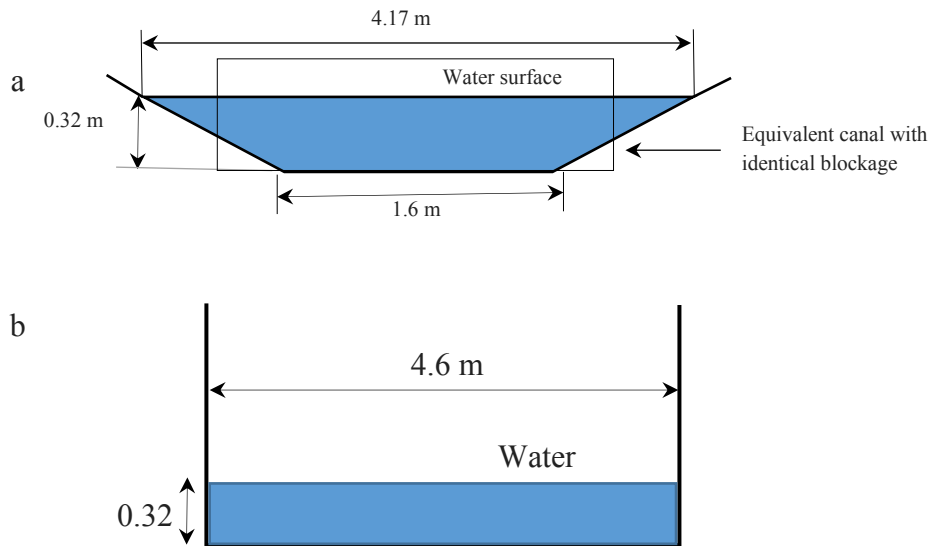


Figure 2. Case-studies: a – Suez Canal case-study, b – rectangular canal

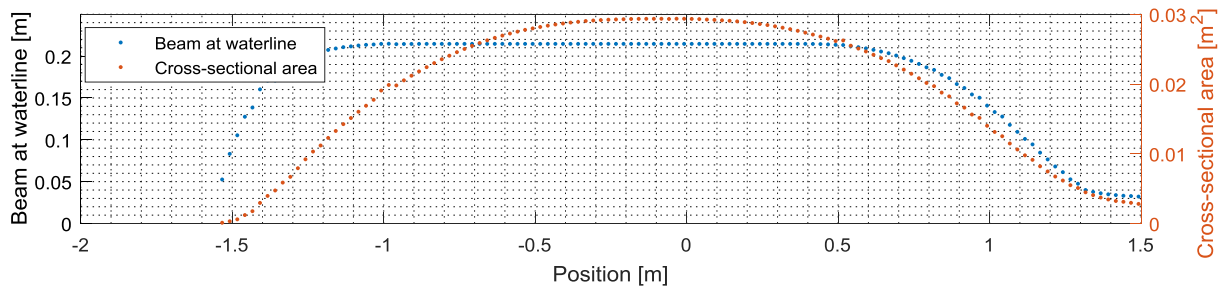


Figure 3. KCS ship model input for slender body calculations

### 3.3 Reynolds-averaged Navier-Stokes

Perhaps the most rapidly developing field in ship hydrodynamics involves the use of Reynolds-averaged Navier-Stokes (RANS) methods. These solve for the 3D fully nonlinear viscous flow around the ship. The rapid development of supercomputers, coupled with the RANS method's ability to resolve complex flow phenomena with good accuracy has meant that many researchers have adopted the RANS method in their toolkit.

In this study, the rectangular canal depicted in Figure 2 is modelled. Naturally, the speeds examined replicate the model-test parameters. This implies that all ship dimensions and parameters follow those, prescribed during the experimental investigation. The commercial available RANS solver, Star-CCM+, version 13.02.011 is used in this study. Star-CCM+ is a finite-volume based solver, which uses the integral form of the governing equations and divides the computational domain into a finite number of adjoining cells.

For the present investigation, hexahedral cells of minimal skewness are used. This is known to provide superior predictions in ship hydrodynamics when compared to tetrahedral cells (Jones and Clarke, 2010). The mesh is generated via the automatic facilities of Star-CCM+. To accomplish this, the trimmed cell mesher is used to construct all cells outside the immediate vicinity of the ship. The near-wall cells are prescribed via the prism layer meshes, which is set to ensure a  $y^+ < 1$  over the wetted area of the ship. In doing so, high local wall-based Reynolds numbers, which require the use of wall-functions are avoided. This is done in view of the fact that wall functions are incompatible with separation and complex phenomena, such as stagnation and recirculation (Durbin and Pettersson Reif, 2011). The resulting cell numbers can be consulted in Table 1. The generated mesh is depicted in Figure 4 for both case-studies, while the resulting  $y^+$  values distribution on the hull are shown in Figure 5.

The depicted mesh is achieved by imposing concentric volumetric refinements in the vicinity of the ship. In particular, the location where the Kelvin wake is expected has been refined considerably in the rectangular canal case. For the Suez Canal, the refinements are concentrated near the lateral extents of the canal. As will be shown in Section 4, the manner in which the waves interact with the bottom is important. The mesh density required in these areas is increased when compared to other locations. In any case, the mesh in the Suez Canal is sufficiently refined to capture the waves everywhere in the domain. Although this implies that the cell numbers have increased dramatically, as shown in Table 1, the heightened computational effort is considered justified.

Table 1. Cell numbers

Case-study	Simulation type	Number of cells
Rectangular canal	Multiphase	1446076
	Double body	1055015
Suez Canal	Multiphase	1954292
	Double body	1038586

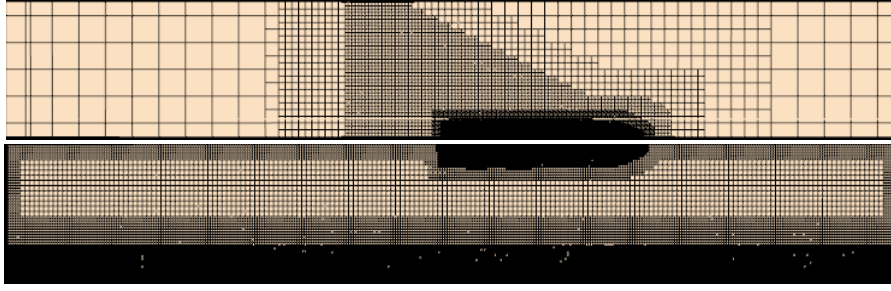


Figure 4. Top view of the generated mesh for the rectangular canal (top half) and Suez Canal (bottom half) – not to scale.

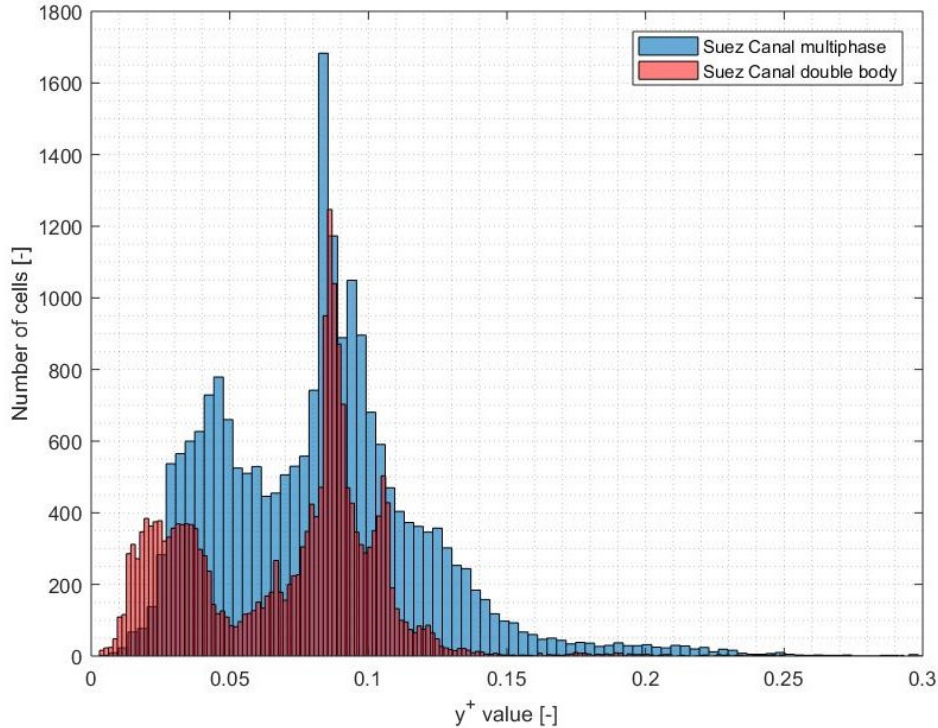


Figure 5. Distribution of  $y^+$  values in multiphase and double body modes for the Suez Canal at  $Fn_h = 0.2439$ .

In terms of numerical set-up, the recommendations of Terziev et al. (2019b) are followed. Namely, a 2<sup>nd</sup> order convection scheme is adopted and the  $k - \omega$  turbulence model is used, which showed reliable predictions over a range of similar case-studies (Terziev et al., 2018; Wilcox, 2006). The  $k - \omega$  turbulence model exhibited good, consistent predictions over a range of case-studies, similar to those examined here. The wall time, required per iteration was also found to be the lowest of all two equation turbulence models, making it a highly attractive choice. Additionally, the  $k - \omega$  turbulence model does not require any modifications if applied near solid boundaries, when attempting to resolve boundary layer phenomena, which govern resistance. The present study will also serve to validate the assertion that the  $k - \omega$  turbulence model provides good predictions over a greater range of case-studies. The expectation is that the resistance will be predicted with a small, negative error based on previous experience

(Terziev et al., 2019b). The temporal term of the Navier-Stokes equations is discretised via a 1<sup>st</sup> order accurate scheme, with a time-step of  $t=0.0035 \times L/V$ , following Tezdogan et al. (2016). In the present simulations, the mesh remains constant for all speeds, while the time step is varied according to the aforementioned formula.

To model ship squat, the Dynamic Fluid Body Interaction (DFBI) module is used. This computes the normal (pressure) forces and tangential (shear or frictional) forces on the ship hull and adjusts its position to achieve equilibrium. In the examined case-studies, only motions in the vertical plane ( $y - z$ ) are allowed. To dampen the initial shock, resulting from the initiation of the simulation, the ship is constrained during the first 10 seconds, which is imposed to allow the flow to develop before the ship is allowed to move. Once this time limit has been overcome, the solver gradually applies forces and moments on the hull during an additional 10 seconds.

The domain dimensions follow the recommendations of the ITTC (2017). While the domain bottom, set as a velocity inlet, and side (slip wall) are prescribed to match the experimental set-up, the domain top is placed at a distance of  $1.5 \times L$  from the undisturbed water surface level. The inlet is also positioned  $1.5 \times L$  upstream of the forward perpendicular, where a velocity inlet condition is imposed. The outlet is located  $2.5 \times L$  ship lengths downstream of the aft perpendicular, and is set to maintain the hydrostatic pressure. To calculate the hydrostatic pressure, model current velocities, and capture free-surface deformations, the Volume of Fluid method is utilised (Hirt and Nichols, 1981). Domain dimensions and boundary conditions are summarised in Figure 6 for the rectangular canal (top) and Suez Canal (bottom).

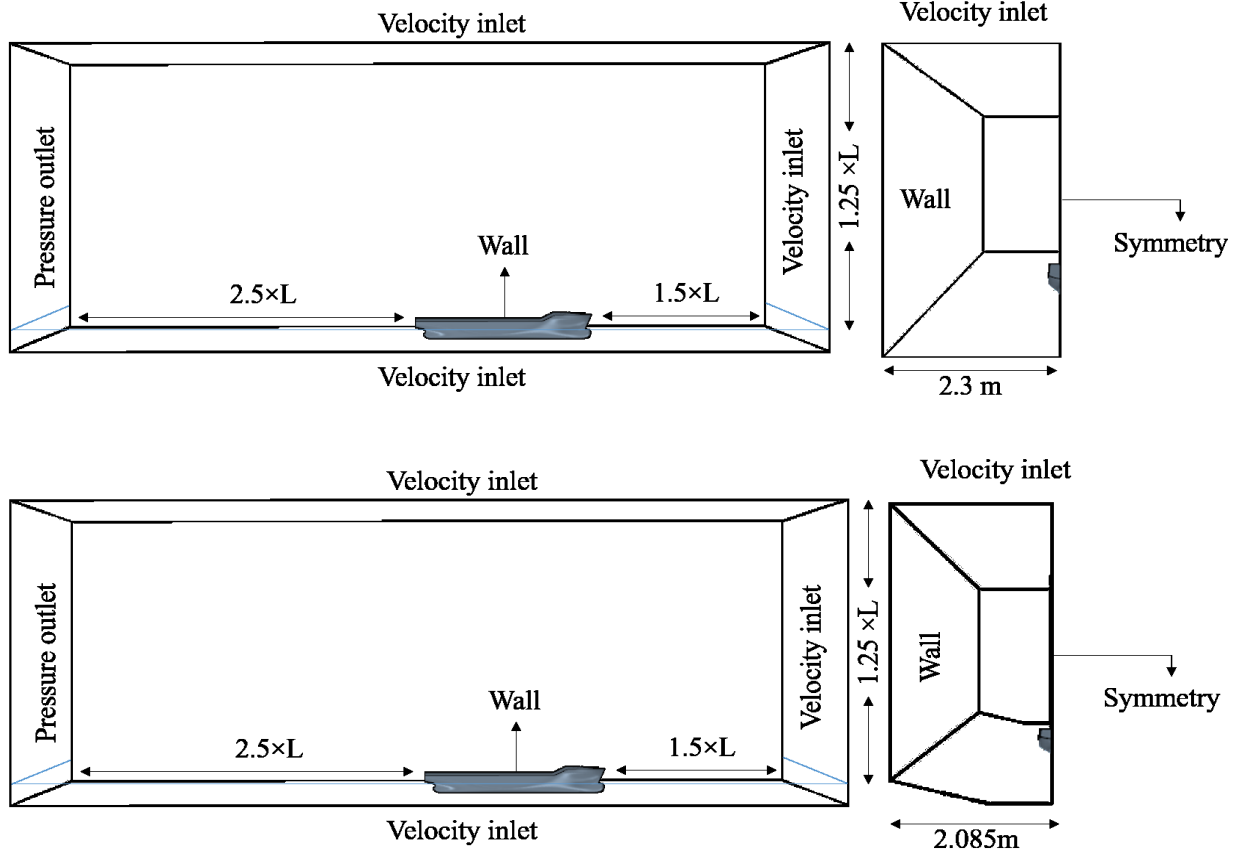


Figure 6. Domain dimensions and boundary conditions in all multiphase simulations. Top: rectangular canal, bottom: Suez Canal (not to scale).

If one seeks to demonstrate changes in the components of ship resistance, a multiphase simulation is insufficient. As mentioned previously, the RANS solver computes forces as normal and tangential. These translate into frictional and pressure resistance coefficients upon division by  $0.5\rho SV^2$ , where  $\rho=997.561 \text{ kg/m}^3$  is the fresh water density,  $S$  is the ship's wetted area, and  $V$  is the ship speed. On the other hand, the resistance extrapolation procedure, endorsed by the ITTC (2017b) decomposes the total differently. Namely, the form factor approach is used, suggested by Hughes (1954), which splits the resistance as shown in Eq. (17).

$$C_T = C_F \times (1 + k) + C_W \quad (17)$$

where  $C_T$  is the total resistance coefficient,  $C_F$  represents the frictional component,  $(1+k)$  is the abovementioned form factor, and  $C_W$  is the wave resistance coefficient.  $C_W$  and  $(1+k)$  are assumed constant with scale, while  $C_F$  is predicted via a friction line (Molland et al., 2017). Since CFD cannot be used to predict all of these components via a multiphase simulation, one may replace the free-surface with a symmetry plane (Kinaci et al., 2016). Essentially, this is equivalent to removing  $C_W$  from Eq. (3), since there are no longer any waves present in the simulation (Farkas et al., 2017). Doing this renders the VOF method inapplicable. For this reason, in double body simulations the velocity is prescribed at the inlet as a constant, while the outlet maintains 0 Pa pressure.

To ensure the flow is dissimilar only due to the absence of waves, the ship's vertical position is adjusted, according to the result obtained by the multiphase simulation (Terziev et al., 2019c). Performing double body simulations allows for the calculation of the wave resistance simply by subtracting the  $C_T$  achieved in multiphase and double body regimes (Min and Kang, 2010). Furthermore, the form factor is simply the double body total resistance, divided by the double body frictional component. These will enable the prediction of changes in  $(1+k)$  and  $C_W$  with speed as well as bathymetry. For the typical cell numbers, achieved for the double body simulations, Table 1 can be consulted.

The double body approach is primarily adopted in this study to determine the wave resistance of the KCS under different conditions. Utilising the resistance decomposition shown in Eq. (17), it is possible to circumvent the complexity of wave resistance estimation. To elaborate, wave resistance estimation in shallow water is a particularly difficult problem. While there are many theories capable of providing an estimate of the sinkage and trim of the ship, resistance in the subcritical range has proved elusive (Beck et al., 1975; Tuck, 1967a, 1966). That is, although deep-water wave resistance can be estimated with the same theory (Tuck and Lazauskas, 2008). Three-dimensional potential flow theories are required to predict ship shallow water wave resistance, which are characterised by a substantial increase in implementation difficulty. For example, Yuan's (2018) method can be used in this respect. However, in the absence of commercially available software, where the above theory has been implemented, one cannot apply it in practice routinely.

The problems associated with wave resistance in shallow water are further magnified by two factors. Firstly, shallow water flows are highly three-dimensional. As demonstrated recently by Terziev et al. (2019b), the boundary layer of the ship is predicted to come in contact with the seabed in very shallow water cases. This brings about the second difficulty, referred to previously, namely, non-linear effects. The presence of such phenomena suggests that the vast majority of shallow water theories are inapplicable, even if they provide non-zero predictions. For instance, the extension of the slender body theory to account for ship-ship interactions of Gourlay (2009) can be supplemented by additional non-linear terms, as shown by Yeung (1978). In fact, the supplementing terms, introduced in the latter reference have been shown to be of similar magnitude as the original terms, formulated by Tuck and Newman (1976).

Non-linearity and three-dimensional effects are not a distinctive problem when it comes in CFD predictions. The RANS equations feature both of the above characteristics. Therefore, CFD can provide insight into the phenomenology of the underlying physics without user intervention, or knowledge of separate linear/non-linear and 2D/3D effects. These are captured automatically in the computational model. In this context, the prediction of the form factor, which is typically used to account for 3D effects is trivial in the presence of data from multiphase and double body simulations. The prediction of the form factor is of importance because of its central role in resistance extrapolation.

In the likely event where the expected routes the ship will spend the majority of its operational lifetime are known, it is of critical importance to predict the full-scale resistance under these conditions. The manner in which this is typically done is via the resistance decomposition,

shown in Eq. (17). Naturally, the use of this relationship requires adequate knowledge of each component on the right-hand side of the equation. As explained previously, wave resistance is associated with a distinct set of challenges. The form factor is also an elusive parameter, which is not sufficiently understood in shallow waters. Frictional resistance in shallow water is also subject to some debate, because as will be shown in Section 4, the ITTC line cannot capture shallow water effects. Zeng et al. (2018) provided a basis for a correction based on the depth over draught ratio ( $h/T$ ), but their formulation is applicable for flat ship bottoms. This is certainly not the case in the vast majority of cases due to the occurrence of ship squat, and is therefore not applied here.

In the presence of continual debate regarding each component of the resistance decomposition shown in Eq. (17), and indeed the relationship itself, it is thought prudent to investigate the RANS solver's performance in predicting these parameters. The availability of experimental data to compare our numerical predictions against is used to establish confidence in the numerical model where appropriate. To the best of our knowledge, form factor and wave resistance studies in shallow waters are few, especially with changing channel cross-section. Thus, the present investigation would serve to supplement knowledge in the field by predicting the expected changes in all factors discussed above.

The results and relevant discussions are given in Section 4, while the following Section provides an overview of the errors and uncertainties induced as a result of the RANS method.

### **3.4 Numerical verification**

As referred to in the previous section, RANS solvers require a time step and grid size to discretise the governing equations temporally and spatially, respectively. The set of partial differential equations, modelled by the solver (the RANS equations) are thought to represent the physics of the problem with sufficient accuracy (Lesieur, 2008). However, this applies to their continuum form, which are solvable and can be used for relatively simple flows. In any case, analytical solutions to the Navier-Stokes equations in three dimensions are rare, and cannot be derived for a problem as complex as multiphase (or double body) flow about a ship hull. For this reason, verification procedures are devised to estimate the error, resulting from either mode of discretisation, and the corresponding uncertainty by extrapolating the solution to a 0 time step or grid size (Roy, 2005). In other words, the solution estimated as if it were possible to model the continuum form of the partial differential equations.

For the present case, the Grid Convergence Index (GCI) method is used, which was devised by Roache (1998) as a uniform method to report numerical uncertainty. This method uses generalised Richardson Extrapolation (Richardson, 1911), and provides a 95% confidence in the computed uncertainty (Roache, 1997). To elaborate, upon estimating the uncertainty, one can have sufficient grounds to maintain that the exact solution lies within the bracket, calculated as the uncertainty. Therefore, the error is defined as a quantity characterised by a magnitude and sign, whereas the uncertainty simple provides an interval, within which the error must be located 95 out of 100 times.

The first step in the verification procedure is to define a refinement ratio ( $r$ ), which is used to magnify the grid size, or time step. Here, the recommendation of the ITTC (2008) are adopted in this respect, namely  $r=\sqrt{2}$ . The refinement ratio is used to generate a triplet of solutions, which are used to predict the numerical error (Celik et al., 2008). Here, it is useful to define the modes of convergence or divergence. These are characterised by the convergence ratio,  $R$ , whose value defines four possibilities:

1. Monotonic convergence:  $\mathbf{0} < \mathbf{R}_\kappa < \mathbf{1}$
2. Oscillatory convergence:  $\mathbf{R}_\kappa < \mathbf{0} \cup |\mathbf{R}_\kappa| < \mathbf{1}$
3. Monotonic divergence,  $\mathbf{R}_\kappa > \mathbf{1}$
4. Undefined error or uncertainty

Where the subscript refers to the  $\kappa^{\text{th}}$  input parameter. In the present context,  $R$  is defined as the ratio of the difference between medium and fine solutions  $\varepsilon_{21} = (\varphi_2 - \varphi_1)$ , and the difference between coarse and medium solutions  $\varepsilon_{32} = (\varphi_3 - \varphi_2)$ . Once these are known, the observed order of accuracy is estimated as shown in Eq. (18):

$$p_\kappa = \frac{\ln(\varepsilon_{\kappa 23} / \varepsilon_{\kappa 21})}{\ln(r_\kappa)} \quad (18)$$

The next step is to predict the extrapolated value, formulated in Eq. (19):

$$\varphi_{ext} = (r_\kappa^p \times \varphi_1 - \varphi_2) / (r_\kappa^p - 1) \quad (19)$$

Then, the approximate relative error and extrapolated relative error are calculated as shown in Eq. (20) and Eq. (21), respectively.

$$e_a^{21} = \left| \frac{\varphi_1 - \varphi_2}{\varphi_1} \right| \quad (20)$$

$$e_{ext}^{21} = \left| \frac{\varphi_{ext}^{21} - \varphi_2}{\varphi_{ext}^{21}} \right| \quad (21)$$

Once the quantities estimated by Eq. (18) – Eq. (21) are known, the uncertainty can be calculated as expressed in Eq. (22):

$$GCI_{fine}^{21} = \left| \frac{1.25 \times e_a^{21}}{r_\kappa^p - 1} \right| \quad (22)$$

The computed data for this case is shown in Table 2, where grid discretisation uncertainty is reported. Table 3 presents estimates of the temporal discretisation-induced uncertainty. The procedure has been carried out for sinkage, trim and total resistance. Since the total is simply the sum of the pressure and shear, it is not thought necessary to extend the reported results for the remaining parameters. The uncertainty analysis presented in this section was performed for the rectangular canal for  $F_h = 0.469$ . This is used as a representative case, providing guidelines in terms of uncertainty for the remaining case-studies.

It is interesting to note that sinkage and trim exhibit super convergence with mesh refinement, but are close to the theoretical order of accuracy ( $p_t=2$ ) when subjected to temporal refinement (Roy, 2005). The opposite is true in terms of resistance.

Table 2. Spatial uncertainty in the rectangular canal,  $F_h = 0.469$ .

	Sinkage (m)	Trim ( $^\circ$ )	Total resistance (N)
$r$ (-)	$\sqrt{2}$	$\sqrt{2}$	$\sqrt{2}$
$\varphi_1$	-0.0052	-0.0675	2.8896
$\varphi_2$	-0.0054	-0.0682	2.9559
$\varphi_3$	-0.0104	-0.0756	3.0935
$R$ (-)	0.04	0.096573	0.4818
$p$ (-)	9.2877	6.7445	2.1068
$\varphi_{ext}^{21}$	-0.005	-0.066831	2.8233
$e_a^{21}$ (%)	0.0192	0.009	0.021
$e_{ext}^{21}$ (%)	0.08	0.0204	0.0469
$GCI_{fine}^{21}$ (%)	7.5321	1.9867	2.463

Table 3. Temporal uncertainty in the rectangular canal,  $F_h = 0.469$

	Sinkage (m)	Trim ( $^\circ$ )	Total resistance (N)
$r$ (-)	$\sqrt{2}$	$\sqrt{2}$	$\sqrt{2}$
$\varphi_1$	-0.0052	-0.0675	2.8896
$\varphi_2$	-0.00517	-0.0674	2.8883
$\varphi_3$	-0.005169	-0.0670	2.8823
$R$ (-)	0.41748	0.50193	0.21667
$p$ (-)	2.5205	1.9889	4.4129
$\varphi_{ext}^{21}$	-0.0051831	-0.067718	2.8909
$e_a^{21}$ (%)	0.00019	0.263	0.045
$e_{ext}^{21}$ (%)	0.059678	0.0111	0.0009
$GCI_{fine}^{21}$ (%)	0.077	0.2926	0.0775

To ensure that the solution has converged sufficiently, the residuals are monitored, requiring a minimum drop of at three orders of magnitude, following the recommendations of the ITTC (2011). To assess iterative errors, the non-intrusive, *a posteriori* method of Roy and Blotner (2001) is used (Phillips, 2012). The results from this analysis indicate that absolute errors are in the range of  $10^{-5} - 10^{-6}$ . To achieve the here reported levels of iterative convergence, the solution is allowed to evolve for a minimum of 200 s physical time. The iterative errors must be several orders of magnitude smaller than the discretisation error to enable the applicability of the GCI (or any other) discretisation uncertainty estimator technique (Eca and Hoekstra, 2014). For the present purposes, this condition is thought to have been satisfied.

#### 4. Results and discussion

In this Section, the results for both case-studies are presented. To facilitate comparison and discussion, the data from all methods are presented jointly for each case-study.

## 4.1 Sinkage and trim

As mentioned previously, sinkage and trim are of great practical importance in restricted waters (Ferguson, 1977). While it is well-known that smaller canal cross-sectional area causes greater ship squat, the manner in which this occurs requires further investigation. The results shown jointly in Figure 8 and Figure 9 demonstrate that the present CFD model agrees well with experimental observations in the rectangular canal. Moreover, the assertion that our CFD model will have a tendency to provide a small negative error is validated for the entire speed range for sinkage in this case-study. In terms of trim, the CFD model has also performed well, predicting values within a reasonable margin. The slender body theory is shown to perform better for trim than for sinkage, as measured at the ship centre of gravity. In any case, the results compare well for low speeds, which is where the slender body theory's strengths lie (Tuck and Taylor, 1970). The apparent disagreement in sinkage for very low speeds is exhibited due to the difficulties in measuring displacements smaller than 2 mm experimentally (Elsherbiny et al., 2019b).

For the rectangular canal, the examined speeds range from 0.1 to 0.57 depth Froude numbers. Although the high speed range is unlikely to occur in practice, it is interesting to note that the disagreements between the CFD and EFD curves in sinkage increase with velocity. On the other hand, the differences in trim remain relatively constant. This implies that sinkage is more difficult to predict than trim using the present CFD model. It is important to keep in mind the experimental uncertainty and its effect on the predicted values. It is important to observe that in the region of practical interest (depth Froude numbers smaller than 0.3), the two sets of data agree well.

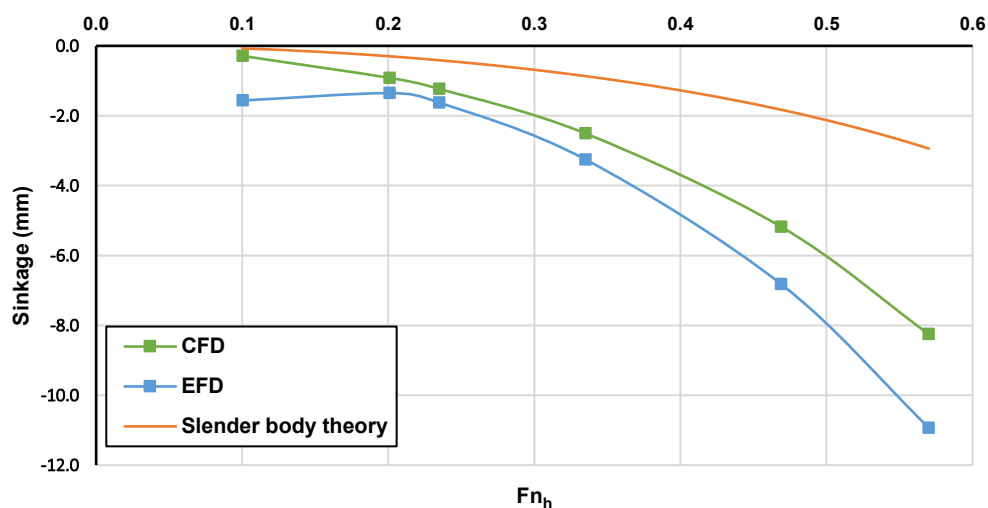


Figure 7. Sinkage for the rectangular canal

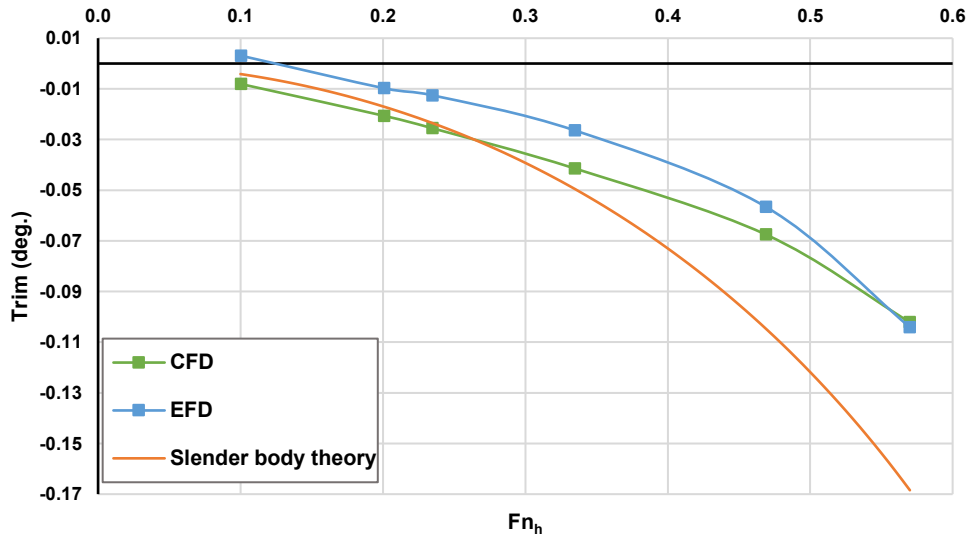


Figure 8. Trim for the rectangular canal

For the Suez Canal, EFD and CFD simulations up to an equivalent of 9 knots in full-scale, which translates to depth Froude numbers between 0.1 to 0.33. This choice is made because the maximum operational speed allowed in the Suez Canal is 7 knots (Suez Canal Authority, 2019). While it is interesting to examine higher speeds for the present case, they cannot occur in practice due to legal restrictions. The current legal restrictions limit the allowable speed, which restricts the number of vessels per year to approximately 18 000. Therefore, the present investigation focuses on practically relevant operational speeds in the Suez Canal. Additionally, Elsherbiny et al. (2019b) demonstrated experimentally that a change in  $h/T$  values within the abovementioned depth Froude number range does not have a significant impact. For this reason, the present study focuses on  $h/T=2.2$  (full-scale depth = 24 m) as a representative case, which translates into the actual full-scale depth of the Suez Canal.

Figure 9 and Figure 10 jointly present the sinkage and trim values obtained for the Suez Canal via CFD, EFD and the slender body theory. The figures indicate that the present CFD model, whose physical modelling characteristics have been carried from the previous case-study, performs adequately in the case of trim. Sinkage once again proves more difficult to accurately estimate. However, the differences between CFD and EFD are smaller than those exhibited by the slender body curves. This may stem from our assumption, that the sloped canal is equivalent to a rectangular canal with equal blockage. More research in this direction is left as future piece of work.

The slope and shape of the slender body curves are governed by several parameters. These include the depth and width of the canal, as well as the shape of the vessel. Additionally, as the depth Froude number approaches unity, a singularity is predicted (Gourlay and Tuck, 2001). In other words, the slope of the slender body prediction will increase until the critical depth Froude number is reached, where it will attain an infinite value. This is not predicted

experimentally or numerically (Elsherbiny et al., 2019b; Terziev et al., 2018), which restricts the applicability of the slender body theory to low speeds.

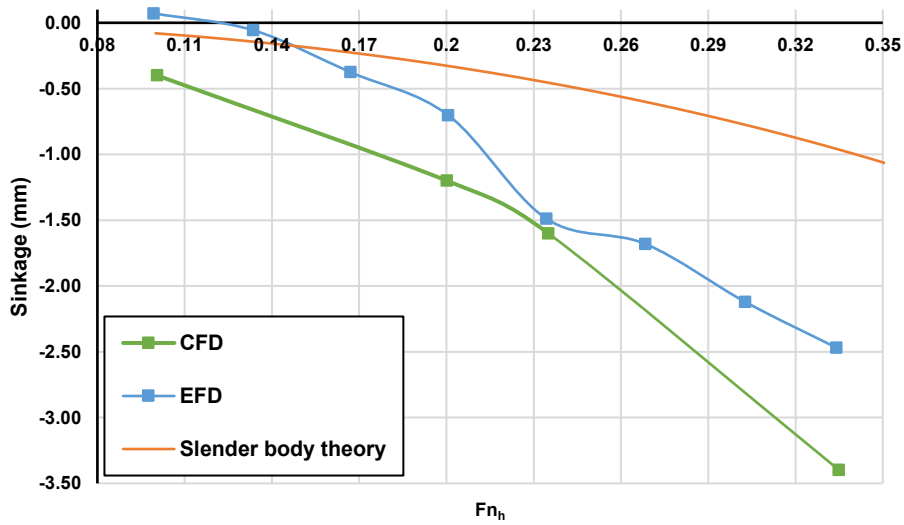


Figure 9. Sinkage for the Suez Canal

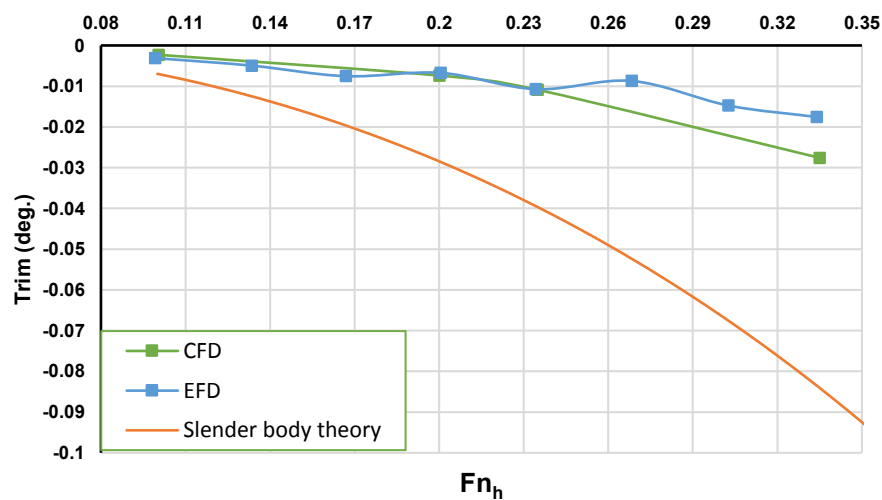


Figure 10. Trim for the Suez Canal

Figure 11 presents a comparison of the measured sinkage values versus the numerical predictions for all case-studies. An apparent pattern, emerging from this figure is that CFD predicts gradual changes in sinkage with the increase of speed. The experimental results show oscillations at certain speeds in the displacement of the centre of gravity of the ship, specifically at  $F_h = 0.303$  for the Suez Canal. Coincidentally, this dip in the measured sinkage matches the numerically predicted sinkage almost exactly. However, once the dip in measured sinkage has been overcome, the apparent difference between the two sets of data begins to increase anew.

An additional observation, made from Figure 11 is that in the rectangular canal case-study, our CFD model underpredicts the sinkage. However, the behaviour of the numerically predicted

values for this parameter are overpredicted in the case of the Suez Canal. This pattern makes the predictions for the Suez Canal match the measured sinkage in the rectangular canal. Conversely, the measured sinkage values in the rectangular canal seem to lie close the Suez Canal, especially in the high speed range. The source of these disagreements is not known. However, one may speculate that a combination of uncertainty, both experimental and numerical, superimposed onto the choices pertaining to the numerics of the CFD model are the source of the disagreements observed above. RANS solutions contain many sources of error, stemming from sources as diverse as boundary conditions, levels of inlet turbulence, iterative and discretisation errors, convection scheme, etc. (Eca et al., 2013; Roy, 2005; Xing and Stern, 2010). Separating each of these components and assessing their impact (when possible) on different aspects of the numerical solution is an ongoing field of research (Eca et al., 2017).

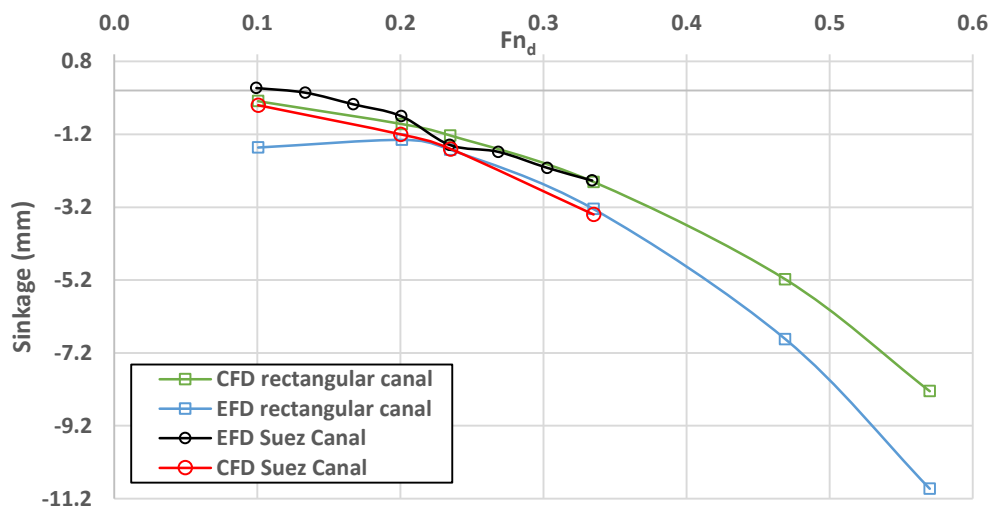


Figure 11. CFD and EFD comparison of sinkage at the ship's centre of gravity for all case-studies

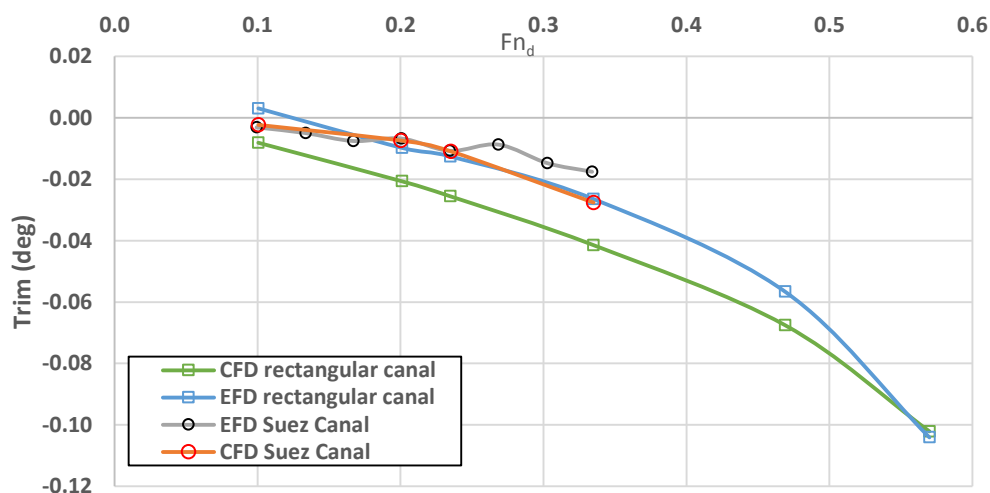


Figure 12. CFD and EFD comparison of ship trim.

The trim predictions, shown in Figure 12 exhibit a different pattern than the sinkage (Figure 11). Although an agreement is observed in the low speed range, the trend is not continued past  $F_h = 0.235$  for the Suez Canal. The EFD data for trim show the oscillatory patterns discussed previously, whereas the CFD predictions follow a smooth path. The two sets of data in the case of the rectangular canal show better agreement in terms of trend, but not in the exact location along the  $y$  – axis. Instead, the CFD method shows a systematic underprediction. However, due to the sharp decline in the EFD curve, the two sets of data almost coincide for the highest speed examined. That is, although this particular point on the graph ( $F_h = 0.57$ ) is unlikely to occur in practice. The sources of error, discussed in the case of sinkage, carry forward to trim as well. In fact, it is well known that the two parameters (jointly forming ship squat) are intrinsically linked (Shivachev et al., 2017).

Figure 13 depicts a comparison of different empirical models for both case-studies. In the figure, how the different models compare to each other for the same case have been plotted, as well as across case-studies. These reveal that formulae, containing higher powers of the speed, tend to massively overpredict values in the high speed range. For instance, Römisch (1989) contains more terms involving higher powers of the speed than the remaining empirical formulae examined in Figure 13 (Briggs et al., 2009a). The empirical formulae used can be found in the Appendix.

Out of all empirical models compared in Figure 13, only the one due to Ankudinov (whose mathematical basis is explained in detail Briggs (2009) and Briggs and Daggett (2009)), is capable of predicting whether a ship will squat by stern or by bow. Unfortunately, both CFD and EFD methods show that the ship will squat by bow, rather than by stern, which is the prediction made by the abovementioned method. This highlights the need for accurate tools even in the early design stage. This particular formulation predicts virtually identical squat for both case-studies, which make it difficult to distinguish the two curves in Figure 13.

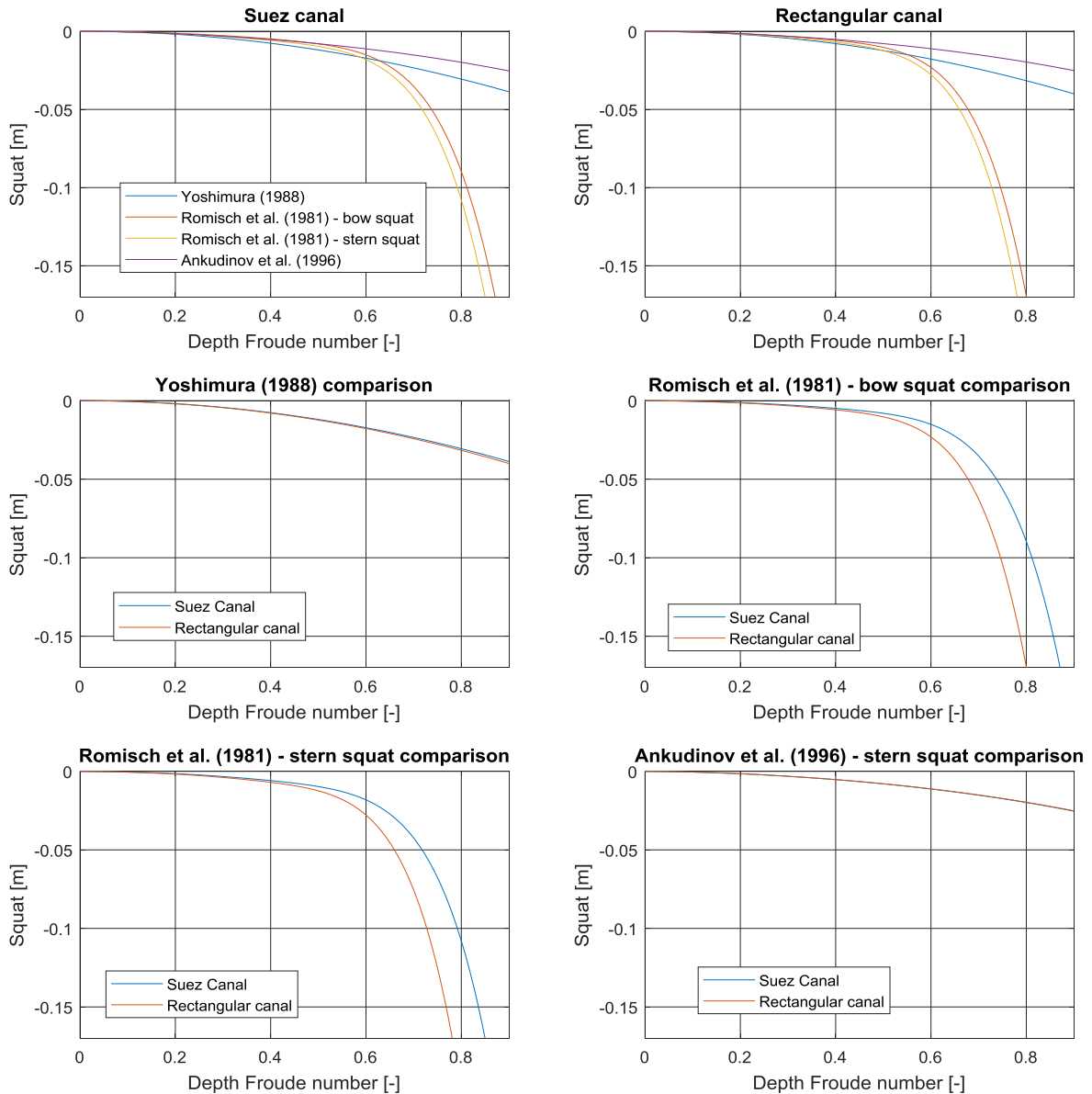


Figure 13. Empirical methods comparison for both case-studies.

## 4.2 Resistance

This section examines the resistance values computed via CFD, EFD and their respective decompositions into constituent components. The discussion begins with the total resistance comparison to establish relative differences between the predicted and measured values.

Over the entire speed range examined for the rectangular canal, the CFD model compares well with the EFD data, as shown in Figure 14. The calculated values show a small underprediction over the majority of the speeds, validating the assertion relating to turbulence modelling. The  $k - \omega$  turbulence model is therefore proven as a good choice for examinations focusing on towed calm shallow water predictions. The resistance values are shown to grow in a quadratic manner with speed, as expected. When comparing these to the Suez Canal, it is evident that the

CFD model does not have a clear tendency to over- or underpredict the EFD data, shown in Figure 15. This is in all likelihood due to the complex nature of the problem.

The CFD method requires the accurate resolution of the free surface to predict the pressure component of resistance. In the rectangular canal this is straightforward. However, the Suez Canal's bathymetry is characterised by a slope, which terminates with an intersection of the water surface. As the waves, shed from the bow approach the bank, they slow down, grow in height and change direction (Lamb, 1932). The manner in which they interact with the bathymetry is not limited to the above. A part of the waves will also reflect back onto the ship upon reaching the beginning of slope, interacting with the hull. Now, the speeds examined for the Suez Canal are low, rendering the waves largely inconsequential near  $Fn_h = 0.1$ . However, as shown in Figure 16, even for a depth Froude number as low as 0.33, the generated disturbance is substantial. The interaction between the ship and the waves, shed from its bow and stern are significant, making this a highly unsteady case.

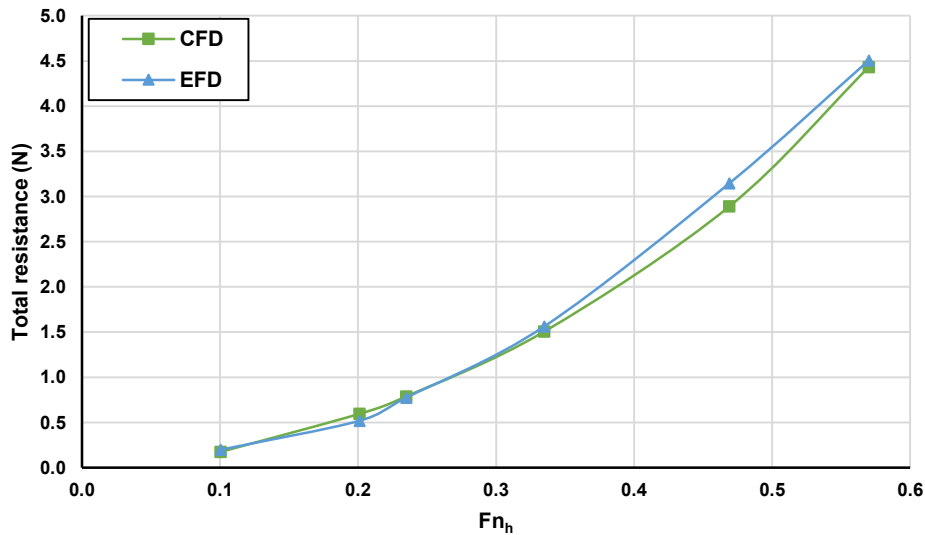


Figure 14. EFD and CFD of total resistance for the rectangular canal

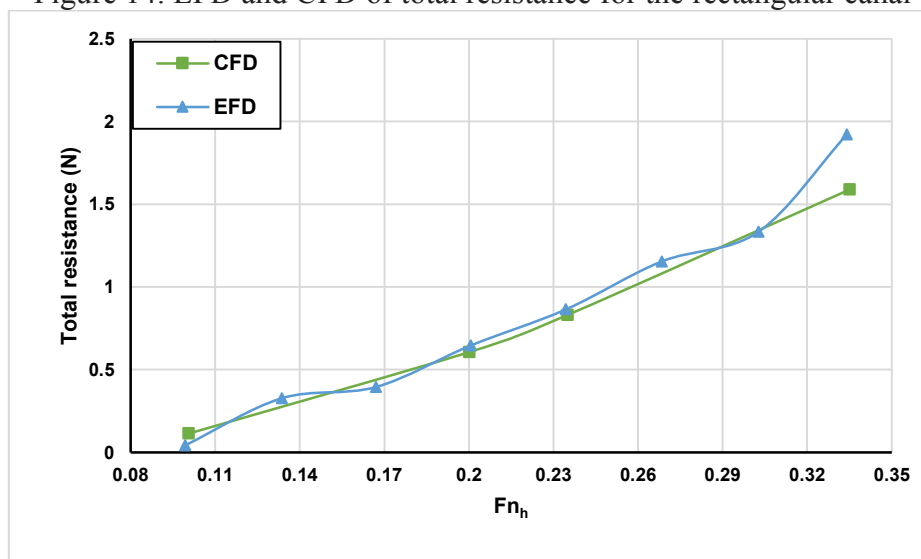


Figure 15. EFD and CFD of total resistance for the Suez Canal

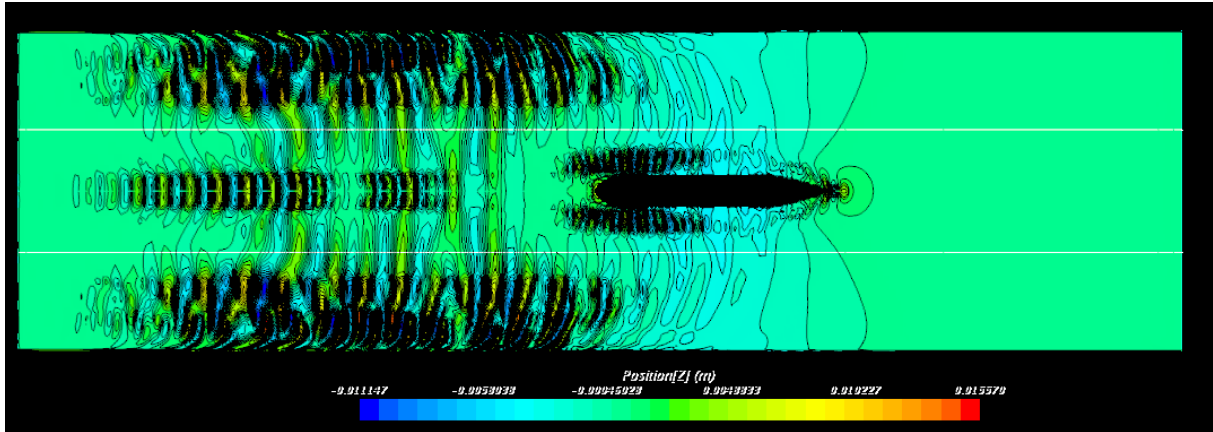


Figure 16. Generated wave patterns in the Suez Canal for  $Fr = 0.33$ . Mirrored about the central plane

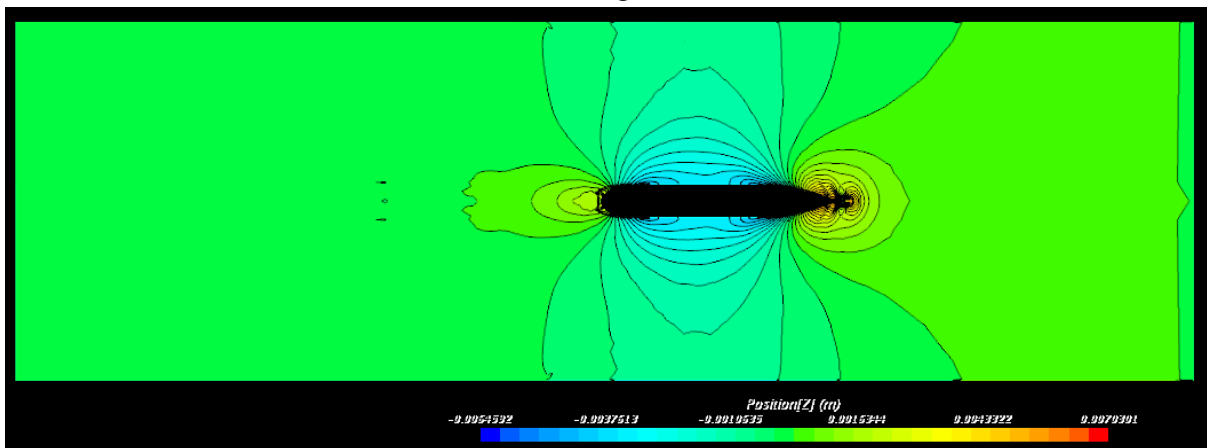


Figure 17. Free surface disturbance, generated in the rectangular canal at  $Fr = 0.33$

In Figure 16, the projection of the beginning of the slope onto the free surface (white lines) have been included to enable a better understanding of the underlying phenomena. In particular, it seems that the seabed immediately after the beginning of the slope does not interact strongly with the waves. This is in line with theoretical predictions, which dictate that the effect on the wave pattern depends on the transition in depth. The large waves, appearing with increasing distance from the ship centreline seem to decompose into smaller components with larger wave heights. According to Newman (1965), the energy within waves vanishes at a rate, proportional to the water depth, and wave heights increase accordingly. This is clearly observed in Figure 16, especially near the banks. No wave breaking is identified in the present case near the lateral extremities of the domain. However, one may expect such phenomena to occur and be visible if the ship speed were to be increased.

It is important to keep in mind that shallow water waves propagate at a speed of  $\sqrt{gh}$ . This explains the observed curve in the shape of the waves as the bank is approached. The propagation speed diminishes with distance from the ship and the waves fall behind (towards

the outlet) at a greater rate than the remaining wave system. The rectangular canal free surface disturbance for the same depth Froude number is shown in Figure 17 for comparison.

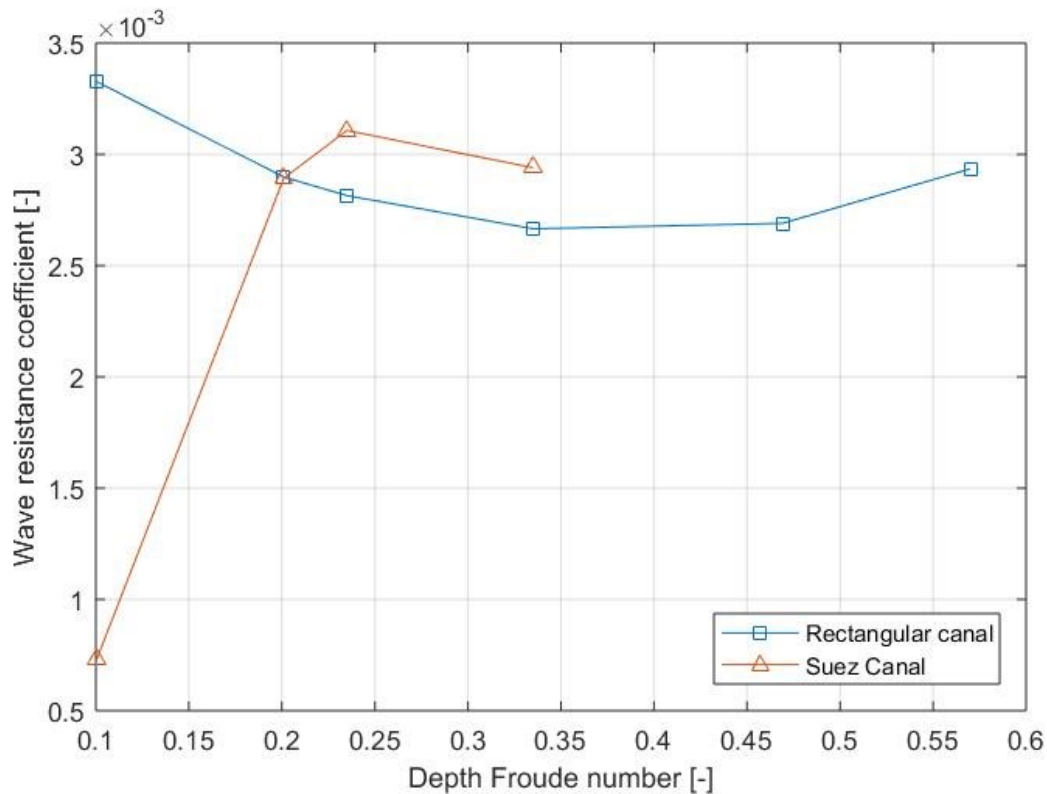


Figure 18. Calculated wave resistance coefficients for both case-studies using CFD

The generated wave patterns induce a wave resistance onto the ship. As explained in Section 4.3, in the present study the wave resistance coefficient is calculated by subtracting the multiphase total from the double body total resistance in CFD. In the rectangular canal, the predicted values show a smooth variation, characterised by an initial decrease, which recovers with increasing depth Froude number (shown in Figure 18). This pattern repeats in all likelihood as one progresses through the depth Froude number range, causing the typical oscillatory pattern of wave resistance to emerge (Tuck and Lazauskas, 2008). The Suez Canal wave resistance on the other hand exhibits a sharp rise, following which, the pattern of the rectangular canal seems to be reproduced. This is not surprising, considering the wave disturbance observed in Figure 17. To elaborate, wave effects become more significant as speed is increased at a greater rate than in the rectangular canal.

The wave resistance coefficients presented in Figure 18 show similar behaviour to those experimentally estimated by Elsherbiny et al. (2019b). However, our predictions are higher than those reported by the abovementioned authors. This can be explained by the choice of friction line, which during the experimental stage (in Elsherbiny et al. (2019b)) was the ITTC line (ITTC, 2017b). The impact of the choice of skin friction coefficient is illustrated in Figure 19. Namely, depending on which method to estimate the skin friction of the ship is chosen, the

wave resistance may vary substantially, especially during the experimental stage, where there is no other choice but to calculate  $C_F$  via a friction line.

Another interesting property of the results presented herein is that in the rectangular canal,  $C_W$  does not show signs of decreasing even when the depth Froude number is as low as 0.1. The Suez Canal results on the other hand exhibit the aforementioned decline. Thus, the zero wave resistance assumption at low speeds may not be valid, depending on the underwater topology.

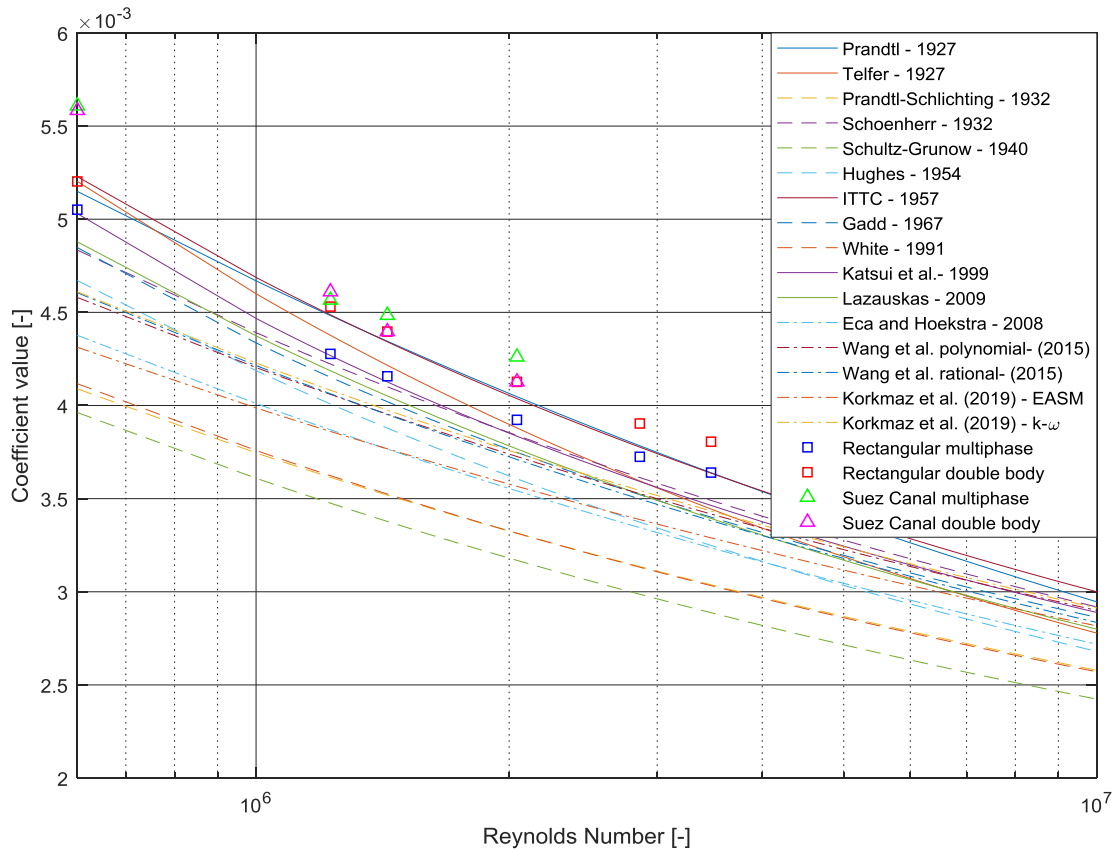


Figure 19. Frictional resistance coefficients for all case-studies (Eca and Hoekstra, 2008; Gadd, 1967; Hughes, 1954; ITTC, 2017b; Katsui et al., 2005; Korkmaz et al., 2019; Lazauskas, 2009; Prandtl, 1925; Schlichting, 1979; Schoenherr, 1932; Schultz-Grunow, 1941; Telfer, 1927; Wang et al., 2015; White, 2006)

In Figure 19, the double body and multiphase frictional resistance coefficients are presented graphically against Reynolds number. Several differences between the case-studies become immediately apparent. Firstly, contrary to the deep water cases of Terziev et al. (2019c), the frictional resistance coefficient in double body mode is higher, rather than lower than the multiphase case for the same Reynolds number in the rectangular canal.

The frictional resistance coefficients predicted for the Suez Canal exhibit a surprising feature. Namely, the double body predictions are either close to, or below the multiphase skin friction predictions. This implies that underwater bathymetry has a substantial effect on  $C_F$ . To further this argument, one may refer to the observed deviation between the frictional predictions for the Suez and rectangular case-studies. Here, it is evident that a lateral restriction creates an

increase in frictional resistance. Thus, the extension of the ITTC line for shallow waters proposed by Zeng et al. (2018), which corrects only the ship bottom, may not be applicable in the present case. In addition, the ship bottom must be maintained flat as part of the abovementioned authors' friction line, which was not done in this study. The difference between  $C_F$  for all cases shows signs of monotonic decline with increasing Reynolds number. This may suggest that free surface effects become negligible at higher speeds or scale factors. However, one must remember that in the resistance calculation process, the underwater area *and* speed are used to non-dimensionalise the resistance coefficients. Thus, an apparent decline in coefficient form could translate into an increase in dimensional resistance, depending on the case.

Figure 20 shows that the form factor behaves in a manner, opposite to the wave resistance for the Suez Canal. That is to say,  $(1+k)$  attains a high value of approximately 1.245 for a depth Froude number of 0.1. This is followed by a sharp decline, which brings the Suez Canal form factor in line with the rectangular canal. In fact, the difference between the two is vanishingly small for the highest depth Froude number examined in the present study. This suggests that, if one were to accept the present resistance decomposition methodology, three dimensional effects decrease in importance with increasing speed. It is also noted that the prediction made herein is virtually the same as in Elsherbiny et al. (2019b) for  $h/T=2.2$ . In fact, it seems that once a speed threshold is passed, the form factor ceases to vary and approaches the experimentally determined value.

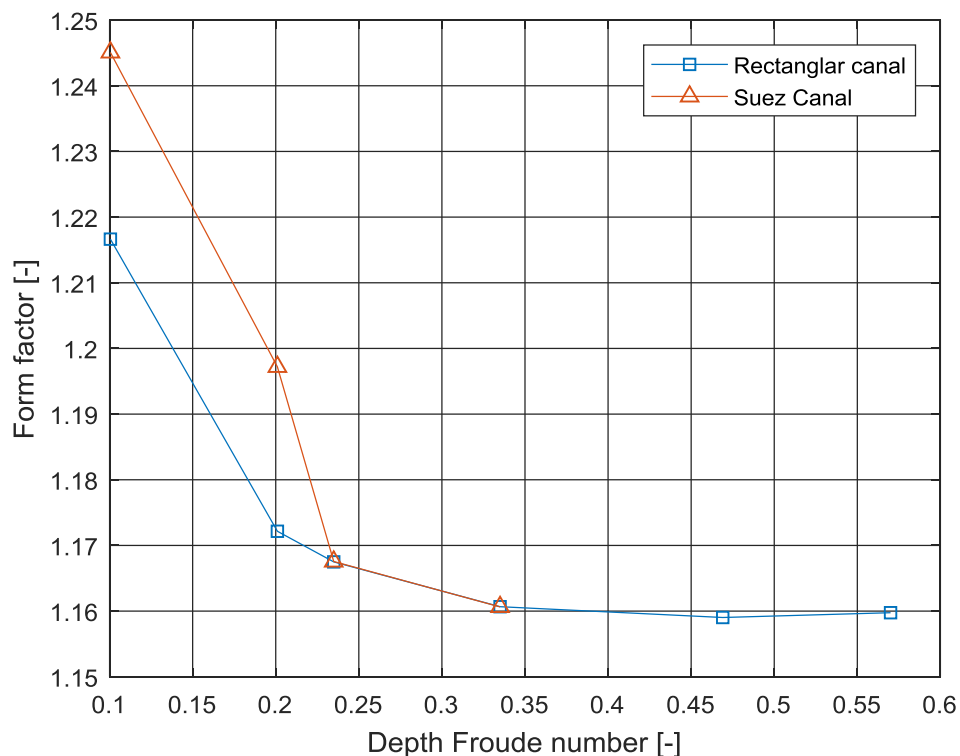


Figure 20. Predicted form factor for all case-studies using CFD

The form factor curve for the rectangular case-study shows a smooth behaviour, which is taken as an indication of the success of the present CFD model. The fact that the Suez Canal

prediction seems to follow a similar path is taken as a good sign in terms of accuracy as well. The apparent disagreement between the two curves for the lowest speed suggests that there may be difficulty in predicting the underlying physics accurately. This is in line with expectations, which dictate that at a very low speed, the waves generated by the ship will be very short. These are difficult to capture if the mesh density is not high in the vicinity of where the abovementioned waves are expected. Although the generated mesh was progressively refined as the bank is approached, this may not have been sufficient for the lowest speeds. However, since the experimental method faces equal, if not greater challenges for the lowest speeds, it is considered that the results presented herein exhibit sufficient levels of accuracy.

The fact that the experimentally determined form factor is close to the low speed predictions of the present CFD model is encouraging. However, it also brings into question the experimental method for determination of the form factor, as applied to canal case-studies. This is typically assessed at very low speeds, where the wave resistance is thought to be negligible. Our findings, specifically Figure 17, demonstrate that wave resistance is likely the cause in the experimental method's inability to predict the change in  $(1+k)$ . As discussed previously, wave resistance does not decay in the rectangular canal as one might expect. The consequence of this is expressed in a contamination of the procedure used to experimentally determine the form factor. The results of this study suggest that CFD should be used to supplement the experimental determination of  $(1+k)$ .

## **5. Conclusion and future work recommendations**

This study presented an experimental and numerical assessment of the effects of bathymetry on ship squat and resistance. To demonstrate the practical importance of the work, the Suez Canal was modelled and compared to a rectangular canal. Emphasis was placed on low and moderate speeds in the Suez Canal, following the legal restrictions imposed on ships in the abovementioned waterway. Specifically, the maximum allowed speed is 7 knots.

In this paper, the numerical results showed best agreement with the experimental data. This is likely the case due to the ability of CFD to model complex phenomena without the need to individually prescribe each term in suitable manner, as is the case for potential flow. With the rapid growth in available computational power, studies such as the one presented here will become frequent. More importantly, the RANS method's ability to provide good predictions when compared to experiments reinforces the case for simulation-based design.

The present investigation focused on changes in form factor, wave resistance and friction across case-studies. The results reveal that the Prohaska test, which requires a vanishingly small wave resistance is valid for the Suez Canal, but may not be true for the rectangular canal. In fact,  $C_W$  vanishes with a reduction in depth Froude numbers below about 0.2. Surprisingly, the rectangular canal's wave resistance showed no signs of decay with low speeds. This suggests that a speed in the vicinity of 0.05 depth Froude number may be required to guarantee that wave effects are asymptotically negligible. Unfortunately, such case-studies are difficult to perform, due to limitations in the sensors used in the course of an experiment. From a numerical

point of view, these case-studies are also challenging. The ship produces short waves, whose resolution requires a much finer mesh than was adopted here.

In terms of form factor, the research, reported above indicates a sharp decline with increasing speed for both case-studies. Our predictions suggest that as the speed is increased, the difference in  $(1+k)$ , calculated for either case vanishes after  $F_h = 0.25$ . In the present cases, the form factor's multiplicative relationship with the frictional resistance coefficient should not be ignored. It is also unlikely that three dimensional effects are captured adequately by a linear resistance decomposition. To support this claim, changes in  $C_F$  between the Suez Canal, rectangular canal, and their double body variants were presented. Surprisingly, the difference between multiphase and double body frictional resistance coefficients was shown to be greater for the rectangular canal than the Suez Canal.

The combination of insurmountable experimental and numerical limitations suggests that it may be more efficient to shift one's attention away from extremely low speeds. These low speeds are used to predict the ship resistance without the influence of wave resistance. In this study, it was demonstrated that this may not be a good approach because wave resistance plays an important role even at very low speeds (near  $F_n=0.1$ ) Instead, the ability of modern computational tools should be exploited to a greater extent, as demonstrated in this study. The numerical method can be used to manipulate the physics of the problem to provide the desired component of ship resistance. Whether it is physically meaningful to split the total into linear components is a disputable matter. In the absence of better extrapolation techniques, one has little choice but to accept the above limitations. However, this is only the case if one continues to view the problem of ship resistance prediction and extrapolation to full-scale as a problem to be approached in a purely experimental way. It is hoped that our study has demonstrated the strong applicability of CFD for problems of practical importance.

The present work could be extended in several ways. The ship's surface was assumed smooth to reduce the complexity of the physics. However, this is rarely, if ever, the case in reality. The variations in skin friction and wave resistance will undoubtedly change upon the inclusion of such effects. For a sample of the intricacies of the subject, the reader is referred to the work of Demirel et al. (2017, 2014), and Song et al. (2019).

Self-propulsion is also an important topic. The presence of a rotating propeller at the stern of the ship causes a complex, unsteady three dimensional pressure field. This affects all aspects of the ship's hydrodynamics (Wang et al., 2017). The shallow water cases examined herein amplify the abovementioned effects in a manner that is not well understood. These problems should be addressed in subsequent studies.

## **Acknowledgements**

Results were obtained using the ARCHIE-WeSt High Performance Computer ([www.archie-west.ac.uk](http://www.archie-west.ac.uk)) based at the University of Strathclyde. The experimental results were obtained at the Kelvin Hydrodynamics Lab at the University of Strathclyde.

## References

- Alderf, N., Leftançois, E., Sergent, P., Debaillon, P., 2008. Dynamic ship response integration for numerical prediction of squat in highly restricted waterways. *Int. J. Numer. Methods Fluids* 601–629. <https://doi.org/10.1002/fld>
- Barrass, C.B., Derrett, D.R., 2012. Chapter 42 – Ship Squat in Open Water and in Confined Channels. *Sh. Stab. Masters Mates* 367–388. <https://doi.org/10.1016/B978-0-08-097093-6.00042-6>
- Beck, R.F., Newman, J.N., Tuck, E.O., 1975. Hydrodynamic forces on ships in dredged channels. *J. Sh. Res.* 19, 166–171.
- Briggs, M.J., 2009. Ankudinov Ship Squat Predictions – Part I: Theory, Parameters, and FORTRAN Programs. *US Army Eng. Res. Dev. Cent.* 1–15.
- Briggs, M.J., 2006. Ship squat predictions for ship/tow simulator (ERDC/CHL CHETN-I-72). *Erdc/Chl Chetn-I-72* 1–18.
- Briggs, M.J., Daggett, L., 2009. Ankudinov Ship Squat Predictions – Part II : Laboratory and Field Comparisons and Validations. *US Army Eng. Res. Dev. Cent.*
- Briggs, M.J., Group, B., Debaillon, P., 2009a. Comparisons of PIANC and Numerical Ship Squat Predictions for Rivers Elbe and Weser.
- Briggs, M.J., Kopp, P.J., Ankudinov, V.K., Silver, A.L., 2013. Comparison of Measured Ship Squat with Numerical and Empirical Methods. *J. Sh. Res.* 57, 73–85. <https://doi.org/10.5957/JOSR.57.1.120007>
- Briggs, M.J., Vantorre, M., Uliczka, K., 2009b. Prediction of Squat for Underkeel Clearance 723–774. [https://doi.org/10.1142/9789812819307\\_0026](https://doi.org/10.1142/9789812819307_0026)
- Calisal, S., Alidadi, M., 2011. A NUMERICAL STUDY ON SQUAT OF A WIGLEY HULL 1–5.
- Celik, I.B., Ghia, U., Roache, P.J., Freitas, C., 2008. Procedure for Estimation and Reporting of Uncertainty Due to Discretization in CFD Applications. *J. Fluids Eng.* 130, 078001. <https://doi.org/10.1115/1.2960953>
- Constantine, T., 1960. On the movement of ships in restricted waterways. *J. Fluid Mech.* 9, 247. <https://doi.org/10.1017/S0022112060001080>
- Dand, W.I., 1967. The wavemaking resistance of ships: Vertical force and form resistance of a hull at uniform velocity. PhD Thesis. University of Glasgow.
- Demirel, Y.K., Khorasanchi, M., Turan, O., Incecik, A., Schultz, M.P., 2014. A CFD model for the frictional resistance prediction of antifouling coatings. *Ocean Eng.* 89, 21–31. <https://doi.org/10.1016/j.oceaneng.2014.07.017>

- Demirel, Y.K., Turan, O., Incecik, A., 2017. Predicting the effect of biofouling on ship resistance using CFD. *Appl. Ocean Res.* 62, 100–118. <https://doi.org/10.1016/j.apor.2016.12.003>
- Duffy, J., 2008. Modelling of Ship-Bank Interaction and Ship Squat for Ship-Handling Simulation by.
- Durbin, P.A., Pettersson Reif, B.A., 2011. Statistical theory and modelling for turbulent flow, Second Edi. ed. Wiley.
- Eca, L., Hoekstra, M., 2014. A procedure for the estimation of the numerical uncertainty of CFD calculations based on grid refinement studies. *J. Comput. Phys.* 262, 104–130. <https://doi.org/10.1016/j.jcp.2014.01.006>
- Eca, L., Hoekstra, M., 2008. The numerical friction line. *J. Mar. Sci. Technol.* 13, 328–345. <https://doi.org/10.1007/s00773-008-0018-1>
- Eca, L., Hoekstra, M., Beja Pedro, J.F., Falcao de Campos, J.A.C., 2013. On the characterization of grid density in grid refinement studies for discretization error estimation. *Int. J. Numer. Methods Fluids* 72, 119–134. <https://doi.org/https://doi.org/10.1002/fld.3737>
- Eca, L., Vaz, G., Hoekstra, M., 2017. Iterative Errors in Unsteady Flow Simulations : Are they Really Negligible ? NuTTS-2017 1–5. <https://doi.org/10.1016/j.cej.2015.03.004>
- el Moctar, O., Shigunov, V., Zorn, T., 2012. Duisburg Test Case : Post-Panamax Container Ship for Benchmarking. *Sh. Technol. Res. J.* 59, 50–64. <https://doi.org/10.1179/str.2012.59.3.004>
- Elsherbiny, K., Tezdogan, T., Kotb, M., Incecik, A., Day, A.H., 2019a. An experimental investigation of the trim effect on the behaviour of a containership in shallow water, in: Proceedings of the ASME 2019 38th International Conference on Ocean, Offshore and Arctic Engineering OMAE2019, Glasgow, UK.
- Elsherbiny, K., Tezdogan, T., Kotb, M., Incecik, A., Day, S., 2019b. Experimental analysis of the squat of ships advancing through the New Suez Canal. *Ocean Eng.* 178, 331–344. <https://doi.org/10.1016/j.oceaneng.2019.02.078>
- Farkas, A., Degiuli, N., Martić, I., 2017. Numerical investigation into the interaction of resistance components for a series 60 catamaran. *Ocean Eng.* 146, 151–169. <https://doi.org/10.1016/j.oceaneng.2017.09.043>
- Ferguson, A.M., 1977. Factors affecting the components of ship resistance. PhD Thesis. University o Glasgow, Department of Naval Architecture. University of Glasgow.
- Gadd, G.E., 1967. A new turbulent friction formulation based on a reappraisal of Hughes' results. *Trans. RINA* 109, 109–511.
- Gourlay, T., 2014. ShallowFlow: A Program to Model Ship Hydrodynamics in Shallow Water, in: OMAE 2014. p. 8. <https://doi.org/10.1115/OMAE2014-23291>
- Gourlay, T., 2009. Sinkage and trim of two ships passing each other on parallel courses. *Ocean Eng.* 36, 1119–1127. <https://doi.org/10.1016/j.oceaneng.2009.06.003>
- Gourlay, T., 2008a. Slender-body methods for predicting ship squat. *Ocean Eng.* 35, 191–200.

<https://doi.org/10.1016/j.oceaneng.2007.09.001>

- Gourlay, T., 2008b. Sinkage and trim of a fast displacement catamaran in shallow water. *J. Sh. Res.* 52, 175–183.
- Gourlay, T., Tuck, E.O., 2001. The maximum sinkage of a ship. *J. Sh. Res.* 45, 50–58.
- Havelock, T., 1924. The Propagation of Groups of Waves in Dispersive Media, with Application to Waves on Water produced by a Travelling Disturbance 422–451. <https://doi.org/10.1098/rspa.1933.0074>
- Hirt, C. W., Nichols, B. D., 1981. Volume of fluid (VOF) method for the dynamics of free boundaries. *J. Comput. Phys.* 39, 201–225. [https://doi.org/10.1016/0021-9991\(81\)90145-5](https://doi.org/10.1016/0021-9991(81)90145-5)
- Hughes, G., 1954. Friction and form resistance in turbulent flow and a proposed formulation for use in model and ship correlation. *Trans. Inst. Nav. Arch.* 96.
- Inui, T., 1954. Wave-Making Resistance in Shallow Sea and in Restricted Water, with Special Reference to its Discontinuities 1, 1–10.
- ITTC, 2017a. Quality System Manual Recommended Procedures and Guidelines Procedure Uncertainty Analysis in CFD Verification and Validation.
- ITTC, 2017b. Recommended Procedures 1978 ITTC Performance Prediction Method, 4th revision, 7.5 – 02 03 – 01.4. 28th Int Towing Tank Conf.
- ITTC, 2011. Recommended Procedures and Guidelines: Practical Guidelines for Ship CFD. 26th Int. Towing Tank Conf.
- ITTC, 2008. Uncertainty Analysis in CFD Verification and Validation Methodology and Procedures. 25th ITTC 2008, Resist. Comm. 12.
- Janssen, P.P., Schijf, J., 1953. The relation between the form of cross section the cross section, the method of revetment and the distribution of the water velocities in a waterway, in: PIANC 18th Congress 1953, Rome, Section SI C1. PIANC.
- Ji, S.C., Ouahsine, A., Smaoui, H., Sergent, P., 2012. 3-D numerical simulation of convoy-generated waves in a restricted waterway. *J. Hydrodyn.* 24, 420–429. [https://doi.org/10.1016/S1001-6058\(11\)60263-1](https://doi.org/10.1016/S1001-6058(11)60263-1)
- Jones, D.A., Clarke, D.B., 2010. Fluent Code Simulation of Flow around a Naval Hull: the DTMB 5415. Def. Sci. Technol. Organ. Victoria (Australia), Marit. platforms Div.
- Joukovski, N., 1903. On the wave of translation. *Complet. Work.*
- Katsui, T., Asai, H., Himeno, Y., Tahara, Y., 2005. The proposal of a new friction line, in: Fifth Osaka Colloquium on Advanced CFD Applications to Ship Flow and Hull Form Design, Osaka, Japan.
- Kinaci, O.K., Sukas, O.F., Bal, S., 2016. Prediction of wave resistance by a Reynolds-averaged Navier-Stokes equation-based computational fluid dynamics approach. *Proc. Inst. Mech. Eng. Part M J. Eng. Marit. Environ.* 230, 531–548. <https://doi.org/10.1177/1475090215599180>
- Korkmaz, K.B., Werner, S., Bensow, R.E., 2019. Numerical friction lines for CFD based form

factor determination, in: VIII International Conference on Computational Methods in Marine Engineering MARINE 2019.

- Kreitner, J., 1934. The Resistance of Ships in Confined Waters. Werft-Rederei-Hafen.
- Lamb, H., 1932. Hydrodynamics. Cambridge Univ. Press 6th revise, 262–264. <https://doi.org/10.1017/CBO9781107415324.004>
- Lataire, E., Vantorre, M., Delefortrie, G., 2012. A prediction method for squat in restricted and unrestricted rectangular fairways. Ocean Eng. 55, 71–80. <https://doi.org/10.1016/j.oceaneng.2012.07.009>
- Lazauskas, L. V, 2009. Resistance, Wave-Making and Wave-Decay of Thin Ships, with Emphasis on the Effects of Viscosity.
- Lesieur, M., 2008. Turbulence in fluids, 4th ed, Physics of Fluids. Springer. <https://doi.org/10.1063/1.1711203>
- Michell, J.H., 1898. The wave-resistance of a ship. London, Edinburgh, Dublin Philos. Mag. J. Sci. 45, 106–123.
- Millward, A., 1996. A review of the prediction of squat in shallow water. J. Navig. 77–88. <https://doi.org/10.1017/S0373463300013126>
- Min, K.-S., Kang, S.-H., 2010. Study on the form factor and full-scale ship resistance. J. Mar. Sci. Technol. 15, 108–118. <https://doi.org/10.1007/s00773-009-0077-y>
- Molland, A.F., Turnock, S.R., Hudson, D.A., 2017. Model-Ship Extrapolation, in: Ship Resistance and Propulsion: Practical Estimation of Ship Propulsive Power. Cambridge University Press, Cambridge, pp. 70–85. <https://doi.org/10.1017/9781316494196.006>
- Newman, J.N., 1965. Propagation of water waves over an infinite step. J. Fluid Mech. 23, 399–415. <https://doi.org/10.1017/S0022112065001453>
- Phillips, T., 2012. Extrapolation-based Discretization Error and Uncertainty Estimation in Computational Fluid Dynamics.
- Prandtl, L., 1925. Report on the investigation of developed turbulence, Translation of “Bericht über Untersuchungen zur ausgebildeten Turbulenz.” Zeitschrift für angewandte Mathematik und Mechanik, vol. 5, no. 2, April 1925.
- Richardson, L.F., 1911. The Approximate Arithmetical Solution by Finite Differences of Physical Problems involving Differential Equations, with an Application to the Stresses in a Masonry Dam. Philos. Trans. th R. Soc. London, Containing Pap. a Math. Phys. Character 210, 307–357.
- Roache, P.J., 1998. Validation and Verification in computational science and engineering. Hermosa Albuquerque, NM.
- Roache, P.J., 1997. Quantification of Uncertainty in Computational Fluid Dynamics. Annu. Rev. Fluid Mech. 29, 123–160. <https://doi.org/10.1146/annurev.fluid.29.1.123>
- Römisch, K., 1989. Empfehlungen zur Bemessung von Hafeneinfahrten. Tech. Univ. Dresden.
- Rotteveel, E., Hekkenberg, R.G., 2015. The Influence of Shallow Water and Hull Form Variations on Inland Ship Resistance 2, 220–236.

- Roy, C., 2005. Review of code and solution verification procedures for computational simulation. *J. Comput. Phys.* 205, 131–156. <https://doi.org/10.1016/j.jcp.2004.10.036>
- Roy, C., Blottner, F.G., 2001. Assessment of One- and Two-Equation Turbulence Models for Hypersonic Transitional Flows. *J. Spacecr. Rockets* 38, 699–710. <https://doi.org/10.2514/2.3755>
- Schlichting, H., 1979. *Boundary-Layer Theory*, 7th ed. McGraw-Hill. <https://doi.org/10.1007/978-3-662-52919-5>
- Schoenherr, K., 1932. Resistance of flat surfaces moving through a fluid. *Trans. Soc. Nav. Arch. Mar. Eng.* 40, 279–313.
- Schultz-Grunow, F., 1941. New frictional resistance law for smooth plates.
- Sergent, P., Lefrançois, E., Mohamad, N., 2015. Virtual bottom for ships sailing in restricted waterways (unsteady squat). *Ocean Eng.* 110, 205–214. <https://doi.org/10.1016/j.oceaneng.2015.10.017>
- Shivachev, E., Khorasanchi, M., Day, A.H., 2017. Trim influence on KRISO container ship (KCS); an experimental and numerical study, in: *Proceedings of the ASME 2017 36th International Conference on Ocean, Offshore and Arctic Engineering*. pp. 1–7. <https://doi.org/10.1115/OMAE2017-61860>
- Song, S., Demirel, Y.K., Atlar, M., 2019. An investigation into the effect of biofouling on the ship hydrodynamic characteristics using CFD. *Ocean Eng.* 175, 122–137. <https://doi.org/10.1016/j.oceaneng.2019.01.056>
- Stern, F., Yang, J., Wang, Z., Sadat-Hosseini, H., Mousaviraad, M., 2013. Computational ship hydrodynamics: Nowadays and way forward. *Int. Shipbuild. Prog.* 60, 3–105. <https://doi.org/10.3233/ISP-130090>
- Suez Canal Authority, 2019. *Suez Canal Rules of Navigation*. <https://doi.org/https://www.suezcanal.gov.eg/English/Navigation/Pages/RulesOfNavigation.aspx>
- Telfer, E. V., 1927. Ship resistance similarity. *Trans. R. Inst. Nav. Archit.* 69, 174–190.
- Terziev, M., Tezdogan, T., Incecik, A., 2019a. Influence of mixed flow on ship hydrodynamics in dredged channels, in: *OMAE2019, Glasgow, UK*. pp. 1–10.
- Terziev, M., Tezdogan, T., Incecik, A., 2019b. Application of eddy-viscosity turbulence models to problems in ship hydrodynamics. *Ships Offshore Struct.* 1–24. <https://doi.org/10.1080/17445302.2019.1661625>
- Terziev, M., Tezdogan, T., Incecik, A., 2019c. In press: A geosim analysis of ship resistance decomposition and scale effects with the aid of CFD. *Appl. Ocean Res.*
- Terziev, M., Tezdogan, T., Oguz, E., Gourlay, T., Demirel, Y.K., Incecik, A., 2018. Numerical investigation of the behaviour and performance of ships advancing through restricted shallow waters. *J. Fluids Struct.* 76, 185–215. <https://doi.org/10.1016/j.jfluidstructs.2017.10.003>
- Tezdogan, T., Demirel, Y.K., Kellett, P., Khorasanchi, M., Incecik, A., Turan, O., 2015. Full-scale unsteady RANS CFD simulations of ship behaviour and performance in head seas

- due to slow steaming. *Ocean Eng.* 97, 186–206.  
<https://doi.org/10.1016/j.oceaneng.2015.01.011>
- Tezdogan, T., Incecik, A., Turan, O., 2016. A numerical investigation of the squat and resistance of ships advancing through a canal using CFD. *J. Mar. Sci. Technol.* 21, 86–101. <https://doi.org/10.1007/s00773-015-0334-1>
- Tuck, E.O., 1967a. Sinkage and Trim in Shallow Water of Finite Width. *Schiffstechnik* 14, 92–94.
- Tuck, E.O., 1967b. A Simple “Filon-Trapezoidal” Rule 121, 1–12.
- Tuck, E.O., 1966. Shallow-Water Flows Past Slender Bodies. *J. Fluid Mech.* 26, 81–95.  
<https://doi.org/10.1017/S0022112066001101>
- Tuck, E.O., Lazauskas, L. V, 2008. Drag on a ship and Michell’s integral, in: 22nd Int. Congress of Theoretical and Applied Mechanics, Adelaide, South Australia, August.
- Tuck, E.O., Newman, J.N., 1976. Hydrodynamic interactions between ships, in: Symposium on Naval Hydrodynamics, 10th, Cambridge, Mass, June 24–28.
- Tuck, E.O., Taylor, J.P., 1970. Shallow wave problems in ship hydrodynamics, in: 8th Symposium Naval Hydrodynamics. pp. 627–659.
- Tunaley, J.K.E., 2014. Ship Wakes in Shallow Waters. LRDC Rep. 6–9.
- Wang, J., Zou, L., Wan, D., 2017. CFD simulations of free running ship under course keeping control. *Ocean Eng.* 141, 450–464. <https://doi.org/10.1016/j.oceaneng.2017.06.052>
- Wang, Z.Z., Xiong, Y., Shi, L.P., Liu, Z.H., 2015. A numerical flat plate friction line and its application. *J. Hydrodyn.* 27, 383–393. [https://doi.org/10.1016/S1001-6058\(15\)60496-6](https://doi.org/10.1016/S1001-6058(15)60496-6)
- White, F., 2006. *Viscous fluid flow*, 3rd ed. McGraw-Hill.
- Wilcox, D.C., 2006. *Turbulence modeling for CFD*, 3rd ed, Transportation Research Record. DCW Industries. <https://doi.org/10.1016/j.aqpro.2013.07.003>
- Xing, T., Stern, F., 2010. Factors of Safety for Richardson Extrapolation. *J. Fluids Eng.* 132, 061403. <https://doi.org/10.1115/1.4001771>
- Yao, J.X., Zou, Z.J., Wang, H.M., 2011. Numerical study on bank effects for a ship sailing in shallow channel. *J. Shanghai Jiaotong Univ.* 16, 91–96. <https://doi.org/10.1007/s12204-011-1100-0>
- Yeung, R.W., 1978. On the interactions of slender ships in shallow water. *J. Fluid Mech.* 85, 143–159. <https://doi.org/10.1017/S0022112078000567>
- Yuan, Z.M., 2018. Ship Hydrodynamics in Confined Waterways. *J. Sh. Res.* 1–14.  
<https://doi.org/http://dx.doi.org/10.5957/JOSR.04170020>
- Zeng, Q., Thill, C., Hekkenberg, R., Rotteveel, E., 2018. A modification of the ITTC57 correlation line for shallow water. *J. Mar. Sci. Technol.* 0, 0.  
<https://doi.org/10.1007/s00773-018-0578-7>
- Zeraatgar, H., Vakilabadi, K.A., Yousefnejad, R., 2011. Parametric Analysis of Ship Squat in Shallow Water by Model Test. *Brodogradnja* 62, 37–43.

Zhang, S., Tezdogan, T., Zhang, B., Xu, L., Lai, Y., 2018a. Hull form optimisation in waves based on CFD technique. *Ships Offshore Struct.* 13, 149–164. <https://doi.org/10.1080/17445302.2017.1347231>

Zhang, S., Zhang, B., Tezdogan, T., Xu, L., Lai, Y., 2018b. Computational fluid dynamics-based hull form optimization using approximation method. *Eng. Appl. Comput. Fluid Mech.* 12, 74–88. <https://doi.org/10.1080/19942060.2017.1343751>

Zhang, S., Zhang, B., Tezdogan, T., Xu, L., Lai, Y., 2017. Research on bulbous bow optimization based on the improved PSO algorithm. *China Ocean Eng.* 31, 487–494. <https://doi.org/10.1007/s13344-017-0055-9>

## Appendix

Parameter	Symbol	Unit	Formula	Notes
Bow Squat (Barrass, 1981)	$S_b$	$m$	$\frac{C_b S_2^{2/3} V^{2.08}}{30} \quad (7)$	
Velocity return factor	$S_2$	–	$\frac{A_s}{A_c - A_s}$	
Blockage factor	$S$	–	$\frac{A_s}{A_c}$	
Channel cross-sectional area	$A_c$	$m^2$		
Ship cross sectional area	$A_s$	$m^2$		
Bow squat (Eryuzlu and Hausser, 1978)	$S_b$	$m$	$0.113B \left(\frac{1}{h/T}\right)^{0.27} F_d^{1.8} \quad (8)$	
Bow squat (Eryuzlu et al., 1994)	$S_b$	$m$	$0.298 \frac{h^2}{T} \left(\frac{V}{\sqrt{gT}}\right)^{2.289} \left(\frac{h}{T}\right)^{-2.972} K_b \quad (9)$	
Correction factor	$K_b$	–	$\frac{3.1}{\sqrt{W/B}}$ for $W/B < 9.61$ $= 1$ for $W/B \geq 9.61$	For unrestricted channels, use $W_{eff}$
Effective width	$W_{eff}$	$m$	$C_M B = [7.7 + 45(1 - C_{WP})^2] \quad (10)$	
Bow squat (Hooft, 1974)	$S_b$	$m$	$1.96 \frac{\nabla}{L^2} \frac{Fn^2}{\sqrt{1-Fn^2}} \quad (11)$	$\nabla$ is the volumetric displacement
Bow squat (ICORELS, 1980)	$S_b$	$m$	$2.4 \frac{\nabla}{L^2} \frac{Fn^2}{\sqrt{1-Fn^2}}$	
Bow squat (Millward, 1990, Millward, 1992)	$S_b$	$m$	$0.001L(61.7C_b \frac{1}{L/B} - 0.6) \sqrt{\frac{F_d^2}{1-0.9F_d^2}} \quad (12)$	
Bow squat (Römisch et al., 1981)	$S_b$	$m$	$C_V C_F K_T T \quad (13)$	

Stern squat (Römisch et al., 1981)	$S_s$	$m$	$C_V K_T T$ (14)		
Correction factor	$C_V$	–	$8 \left( \frac{V}{V_{CR}} \right)^2 \left[ \left( \left( \frac{V}{V_{CR}} - 0.5 \right)^4 + 0.0625 \right) \right]$ (15)	For ship speed	
Relevant water depth	$h_{mT}$	$m$	$h - \frac{h_m}{h} (h - h_m)$		
Wave celerity	$C_{mT}$	$\frac{m}{s}$	$\sqrt{g h_{mT}}$	Based on the relevant water depth	
Mean water depth	$h_m$	$m$	$\frac{A_c}{W_{Top}}$		
Channel width	$W_{Top}$	$m$	$W + 2nh$	At the water surface	
Correction factor for the ship's shape	$C_F$	–	$\left( \frac{10c_b}{L/B} \right)^2$	= 1 for stern squat	
Correction factor	$K_T$	–	$0.155 \sqrt{h/T}$	For squat at critical speeds	
Wave celerity	$C$	$\frac{m}{s}$	$\sqrt{gh}$	Based on the depth $h$	
Inverse bank slope	$n$	–	–	Specified as an integer	
Ship critical speed	$V_{CR}$	$\frac{m}{s}$	$V_{CR} = CK_{ch}$	$U$ configurations	
			$V_{CR} = CK_C$	$R$ configurations	
			$V_{CR} = C_{mT} \left[ K_{ch} \left( 1 - \frac{h_m}{h} + K_c \left( \frac{h_m}{h} \right) \right) \right]$	$C$ configurations	
Correction factor	$K_c$	–	$0.2306 \log \left( \frac{1}{s} \right) + 0.0447$		
Wave celerity	$C_{mT}$	$\frac{m}{s}$	$\sqrt{g h_{mT}}$	Based on the relevant water depth $h_{mT}$	
Bow/Stern squat (Ankudinov et al., 1996)	$S_{Max}$	$m$	$L(S_{mid} \pm 0.5Trim)$ (16)	+ 0.5Trim : Bow	<b>Bow/Stern squat depends on trim (+/-). For <math>F_d \leq 0.6</math></b>
				– 0.5Trim : Stern	
Midship sinkage (Ankudinov et al., 1996)	$S_{mid}$	$m$	$(1 + K_P^S) P_{Hu} P_{F_d} P_{+h/T} P_{Ch1}$ (17)	<b>For <math>F_d \leq 0.6</math></b>	

Factor	$K_p^S$	-	0.15	Ships with single propellers
			0.13	Ships with twin propellers
Hull parameter	$P_{Hu}$	-	$1.7C_B \left(\frac{BT}{L^2}\right) + 0.004C_B^2$	
Forward speed parameter	$P_{Fd}$	-	$F_d^{1.8+0.4F_d}$	
Water depths effect parameter	$P_{+h/T}$	-	$01 + \frac{0.35}{(h/T)^2}$	
Channel effects parameter	$P_{Ch1}$	-	1	<i>U</i> configurations
			$1 + 10S_h - 1.5(1 + S_h)\sqrt{S_h}$	<i>R</i> and <i>C</i> configurations
Water depth factor	$S_h$	-	$C_B \left(\frac{s}{h/T}\right) \left(\frac{hT}{h}\right)$	<i>R</i> and <i>C</i> configurations
Trim (Ankudinov et al., 1996)	<i>Trim</i>	°	$-1.7P_{Hu}P_{Fd}P_{h/T}K_{Tr}P_{Ch2}$	
Trim coefficient	$K_{Tr}$	-	$C_b^{n_{Tr}} - (0.15K_p^S + K_p^T) - (K_B^T + K_{Tr}^T + K_{T1}^T)$	
Trim exponent	$n_{TR}$	-	$2 + 0.8P_{Ch1}/C_b$	
Propeller parameter	$K_p^T$	-	0.15	Single propellers
			0.2	Twin propellers
Bulbous bow parameter	$K_B^T$	-	0.1	Ships with bulbous bows
			0	Ships without bulbous bows
Stern transom parameter	$K_{Tr}^T$	-	0.04	Ships with a stern transom
			0	Ships without a stern transom
Initial trim factor	$K_{T1}^T$	-	$\frac{T_{ap}-T_{fp}}{T_{ap}+T_{fp}}$	
Trim correction parameter	$P_{Ch2}$	-	1	<i>U</i> configurations
			$1 - 5S_h$	<i>R</i> and <i>C</i> configurations
Bow squat (Yoshimura, 1988)	$S_b$	<i>m</i>	$\frac{\left[\left(0.7 + \frac{1.5T}{h}\right)\left(\frac{BC_b}{L}\right) + \frac{15T}{h}\left(\frac{BC_b}{L}\right)^3\right]V_e^2}{g}$	<i>U</i> , <i>R</i> and <i>C</i> configurations $g = 9.81m/s$
Enhanced ship speed term	$V_e$	$\frac{m}{s}$	$\frac{v}{1-s}$	

The information, presented in this Appendix has been adopted form Terziev et al. (2018).